

# AstroSat View of Transient Low-mass X-ray Binary XTE J1701-462: Spectral and Temporal Evolution along the Z-track

Vivek K. Agrawal

Space Astronomy Group, U. R. Rao Satellite Centre, Bangalore, 560037, Karnataka, India

Author for correspondence: Vivek K. Agrawal, Email: vivekag@ursc.gov.in.

## Abstract

*AstroSat* observed transient neutron star low-mass X-ray binary XTE J1701-462 for a total duration of  $\sim 135$  ks during its 2022 outburst. We report the results of a detailed spectral and timing analysis carried out using this data. The source traced a complete 'Z' shaped structure in the hardness intensity diagram (HID). The source exhibited an extended horizontal branch and a short-dipping flaring branch in the HID. The spectra of the source were fitted with different approaches. We find that most suitable spectral model comprises emission from a standard multi-color accretion disk (diskbb in XSPEC) and Comptonized radiation from a hot central corona, described by *Comptb* model of XSPEC. The observed disk component is cool, having a temperature in the range of  $\sim 0.28 - 0.42$  keV and truncated far ( $\sim 250 - 1600$  km) from the compact object. The Compton corona has an optical depth in the range of  $\sim 3.4 - 5.1$  and a temperature in the range of  $3.3 - 4.5$  keV. The disk and corona flux as well as truncation radius vary significantly along the HID. The temperature  $kT_{in}$  depends on both luminosity and inner disk radius and hence shows marginal variation as compared to the truncation radius. We discuss possible scenarios to explain the relationship between the spectral evolution and motion of the source along the HID. The timing analysis revealed horizontal branch oscillations (HBOs) in the frequency range  $\sim 34 - 40$  Hz. The frequency and rms strength of HBO vary systematically as the source moves along the horizontal branch (HB). The observed correlation of the HBO properties with the position on the HB is similar to that previously reported in this source using *RXTE* data during the 2006 outburst of the source. The source also showed normal branch oscillations (NBOs) with frequency  $\sim 6.7$  Hz in the middle and the lower normal branch. The energy-dependent study of the HBO properties suggests that the HBO is stronger in the higher energy band. We also observed very-low frequency noise (VLFN) and band-limited noise (BLN) components in the power density spectra. The break frequency of BLN component was found to be tightly correlated with the HBO frequency. We discuss possible models to explain the origin and nature of the observed features in the PDS.

**Keywords:** accretion, accretion discs - X-rays: binaries - X-rays: individual: XTE J1701-462

## 1. Introduction

A low magnetic field neutron star (NS) accreting material from a low mass companion star provides a way to understand the complex accretion and emission processes close to the ultra-dense star. X-ray flux and spectral-timing properties of neutron star low-mass X-ray binaries (NS-LMXBs) vary on time scales of hours to months causing them to trace different patterns on the color-color (CCD) and hardness-intensity diagram (HID). The most luminous and persistent NS-LMXBs, known as Z-sources trace a pattern that resembles an approximate 'Z' shape. Three distinct branches of the Z-pattern are horizontal branch (HB), normal branch (NB) and flaring branch (FB). Major fractions of the NS-LMXBs trace a fragmented pattern, consisting of a curved banana branch and an island type structure (Hasinger and van der Klis 1989). Z-sources have luminosity in the range of  $0.5 - 1.0 L_{Edd}$ , while luminosity of atoll sources vary in the range of  $0.01 - 0.2 L_{Edd}$  (Barret 2001). It has been argued that mass accretion rate increases as Z-sources move from the HB to the NB and then to the FB (Hasinger et al. 1990). There are six Galactic persistent Z-sources (Hasinger and van der Klis 1989), one extra-galactic Z-source (Smale and Kuulkers 2000) and one transient Z-source (Homan et al. 2007). GX 13+1 and Cir X-1 is also considered as candidate Z-sources (Shirey, Bradt, and Levine 1999; Schnerr et al. 2003; Fridriksson, Homan,

and Remillard 2015). The neutron star transient source IGR J17480-2446 also showed both 'Z' and 'atoll' like behavior (Chakraborty, Bhattacharyya, and Mukherjee 2011).

The energy spectra of Z-sources are soft in nature and consist of two main emission components. Most prominent components are, a cool Comptonized emission from a corona and a thermal emission from a multi temperature accretion disk or a boundary-layer around the NS (Di Salvo et al. 2001; Di Salvo et al. 2002; Iaria et al. 2004; Agrawal, Nandi, and Ramadevi 2020; Agrawal and Nandi 2020). An exact nature of the soft component, geometry and location of the corona that produces the Comptonized emission by inverse Compton process are still under debate. In some cases, other than two main spectral components, a signature of reflection of the coronal emission from an accretion disk (Coughenour et al. 2018; Ludlam et al. 2022) is also seen. A high energy tail is also found to be present in the spectra of the Z-sources (Di Salvo et al. 2001; Di Salvo et al. 2002; Agrawal, Nandi, and Ramadevi 2020). The atoll sources exhibit two spectral states, high-soft and low-hard. In the high-soft state the spectra of these sources resemble those of Z-sources. However in the low-hard state the spectra has Comptonized component with temperature  $\sim 10 - 30$  keV (Barret et al. 2000; Gierliński and Done 2002).

Low Frequency Quasi-periodic Oscillations (LFQPOs) in

the frequency range 5–70 Hz have been observed in the power density spectra (PDS) of Z-sources (van der Klis 2006). In Z-sources, the centroid frequency and other properties of the LFQPOs show a strong dependence on the position of the source on the HID and CCD. Horizontal branch oscillations (HBOs) with a frequency  $\sim 10 - 70$  Hz, normal branch oscillations (NBOs) with a frequency 5–10 Hz and flaring branch oscillations (FBOs) with centroid frequency  $\sim 20$  Hz are seen in the HB, NB and FB respectively (Homan et al. 2002; P. G. Jonker et al. 2002). FBOs and NBOs are connected and possibly have a same origin. Many competing models exist to explain the origin of the LFQPOs. However, the mechanism that can explain all the observed properties of these features is not fully understood.

XTE J1701–462 is the first Z-source that shows transient behavior (Homan et al. 2007). It has undergone two outbursts, the first one on 2006 January 18 (Remillard et al. 2006). The second outburst was detected on 2022 September 6 by MAXI/GSC (Iwakiri et al. 2022). During the first outburst the source evolved from a Cyg-like Z-source to a Sco-like Z-source and then finally at the end of the outburst it displayed an atoll-like behavior (Lin, Remillard, and Homan 2009). Main difference between the Cyg-like and the Sco-like Z-sources are the shape of their Z-tracks. The Cyg-like sources have an extended and a horizontal HB, while the Sco-like Z-sources have a slanted HB. Lin, Remillard, and Homan (2009) used a model consisting of a single temperature black-body (BB), a multi-color-disk-blackbody (MCD) emission and a constrained broken power-law (CBPL) to describe the X-ray spectra of this source during various stages of its outburst. A detailed spectral evolution study was performed by Ding et al. (2011) employing the model used by Lin, Remillard, and Homan (2009). Three type-I X-ray bursts were reported in the source during 2006–2007 outburst (Lin et al. 2009). Using the photospheric expansion burst a distance to the source was estimated to be 8.8 kpc (Lin et al. 2009). The HBOs with a frequency  $\sim 10-60$  Hz and the NBOs with a frequency  $\sim 7-10$  Hz have been observed in the source (Homan et al. 2010; Homan et al. 2007). Moreover, pairs of kHz QPOs are observed during the Z-stage of the source (Sanna et al. 2010). X-ray polarization with a polarization degree  $\sim 4.5\%$  and a polarization angle  $\sim 143^\circ$  has been detected in the source. (Cocchi et al. 2023; Jayasurya, Agrawal, and Chatterjee 2023). The recent X-ray spectro-polarimetric study carried out using the simultaneous data from *IXPE*, *NuSTAR* and *Insight-HXMT* showed that degree of polarization decreases as the source moves from HB to NB (Yu, Bu, Doroshenko, et al. 2024).

In this work, we have carried out spectral and temporal studies of the low-mass X-ray binary XTE J1701–462 during its 2022 outburst using the *AstroSat* data. The HID revealed a pronounced HB and a dipping FB. A detailed spectral and temporal evolution study has been carried out to understand the origin of the Z-pattern and the power-spectral features. The HBOs and NBOs are found to be present in the power density spectra. The remainder of the paper is arranged in the following manner. Section 2 gives the details of observation and the procedures of data reduction. Section 3 provides a

description of the methods adopted to carry out spectral and temporal data analysis. Results of the analysis are presented in the section 4. Finally, we explain the results obtained by the analysis in section 5.

## 2. Observation and Data Reduction

*AstroSat* observed the source XTE J1701–462 from 2022 September 25 to 2022 September 26 (Obs A) and from 2022 October 1 to 2022 October 3 (Obs B) during its 2022 outburst. The source was observed for a net exposure time of 50 ks during Obs A and 85 ks during Obs B. The data collected from Soft X-ray Telescope (*SXT*) and Large Area X-ray Proportional Counters (*LAXPC*) on-board *AstroSat* were used in the present work. *SXT* carries X-ray optics and a focal plane imager that is sensitive in the energy band 0.3–8.0 keV (Singh et al. 2016). There are three *LAXPC* units: *LAXPC10*, *LAXPC20* and *LAXPC30*. These units operate in the energy range 3–80 keV (Yadav et al. 2016). During the observation, *LAXPC* units were operated in the event analysis mode that has time tagging accuracy of 10 micro seconds. *SXT* has two different operational modes, photon counting mode and fast-window (FW) mode. In the photon counting mode the entire frame is read out in 2.38s whereas in the FW mode the central  $150 \times 150$  pixels are selected and read out in 278 ms. During Obs A, *SXT* was operated in the photon counting mode and the FW mode was used to collect data during the Obs B. *LAXPC* data reduction was performed using the latest version of software package *LAXPCSOFT*<sup>a</sup>. This software creates standard products such as lightcurves and spectra using *LAXPC* level-1 products. *XSELECT* software version 2.5 is used to generate the image, spectra and lightcurves from *SXT* Level-2 data. The count rate of the source exceeds the pileup limit ( $> 40$  counts/s; see Malu et al. 2021) and hence we exclude events from the central 2 arc minute of the *SXT* image. We extract the *SXT* spectra from an annular region with inner radius of 2 arc-minute and outer radius of 12 arc-minute. The *SXT* image marked with selection region has been shown in Figure 1. The latest version of the response matrices are used to analyze the spectra of *LAXPC* and *SXT*. The Ancillary Response File (ARF) for the *SXT* is created using the task *sxtARFModule*<sup>b</sup>.

## 3. Data Analysis

### 3.1 Generation of HID and Lightcurve

Since the *LAXPC20* unit has a stable gain, we used the events from this unit to create the lightcurve and HID. The task *laxpc11* of *LAXPCSOFT* package is used to generate the source and background lightcurves as well as spectra. The background level for *LAXPC20* in the energy band 3–30 keV during our observations was  $\sim 70-80$  counts/s. The time bin size used to extract the lightcurve is 256s. We have combined both Obs A and Obs B while generating the lightcurve. We have plotted the *MAXI* lightcurve in the energy band 2–20 keV in Figure

a. [https://www.tifr.res.in/asrosat\\_laxpc/LaxpcSoft.html](https://www.tifr.res.in/asrosat_laxpc/LaxpcSoft.html)

b. [https://www.tifr.res.in/astrosat\\_sxt/dataanalysis.html](https://www.tifr.res.in/astrosat_sxt/dataanalysis.html)

2. In Figure 2, the LAXPC lightcurve in the energy band 3–60 keV and variation in the LAXPC hardness ratio are also shown as inset. Here, the LAXPC hardness ratio is defined as ratio of count rates in the energy bands 9.7–20 keV and 4.6–9.7 keV. The Obs A and Obs B are marked with two vertical lines in the figure. In addition we have also plotted the hardness ratio for the *MAXI* observations and LAXPC observations. It is clear from the Figure 2 that both *AstroSat* observations took place close to peak of the outburst. We have also marked the position of dipping FB (FB2) in the inset figure using vertical lines. The hardness ratio for the *MAXI* observations are defined as ratio of count rates in the energy bands 10–20 keV and 4–10 keV. The *LAXPC20* lightcurves in the energy ranges 6.5–9.7 keV, 9.7–20 keV and 3–20 keV are used to generate the HID. In the HID ratio of the count rates in the energy bands 9.7–20 keV and 6.5–9.7 keV are plotted against intensity in the 3–20 keV energy band. In Figure 3 we show the HID of the source, where each point corresponds to a 256s bin size. HID has an extended HB and a less prominent dipping FB. The different regions of the Z-track are marked with boxes. We extract the spectra and the power-density spectra (PDS) corresponding to these sections to study their evolution along the HID. The HB has been divided in four segments: HB1, HB2, HB3, HB4. The NB has four sections: NB1, NB2, NB3, NB4. The FB is divided in FB1 and FB2. We also created CCD using lightcurves in energy bands 3.0–4.6 keV, 4.6–6.5 keV, 6.5–9.7 keV and 9.7–20 keV. The soft colors are calculated by taking ratio of the count rate in the energy bands 4.6–6.5 keV and 3.0–4.6 keV and the hard color is computed by taking ratio of the count rate in the energy bands 6.5–9.7 keV and 9.7–20 keV bands. We show the CCD of the source in Figure 4.

### 3.2 Analysis of Spectroscopic data

X-ray spectra using the *LAXPC20* data and the *SXT* data were extracted for all the ten segments of the HID. These spectra were modeled and analyzed using XSPEC version 12.13. We consider the *LAXPC20* data up to 30 keV for the spectral fitting due to limited statistics above 30 keV and dominance of the background at higher energies. The *SXT* data in the energy range 0.7–7 keV are used for the combined spectral fitting. The combined broad band spectra in the energy band 0.7–30 keV are fitted with the three different approaches. First we used the combination of a MCD (*diskbb* in XSPEC) and a simple blackbody (BB) emission (*bbbodyrad* in XSPEC). The model MCD+BB (hereafter **Model 1**) has been used previously to model the spectra of this source (Lin, Remillard, and Homan 2009) and emission in the soft state of two atoll sources (Lin, Remillard, and Homan 2007). We also added a constrained broken power-law (CBPL) component to the Model 1 following Lin, Remillard, and Homan (2009). The photon index ( $\Gamma_1$ ) was frozen to a value 2.5 and break energy ( $E_{break}$ ) was fixed at 20 keV. The second power-law index was frozen to the best fit values. Only normalization of CBPL was left free. The model improves the fit for HB1, HB2 and HB3.

However, for other sections of the Z-track addition of this component did not improve the fit. Hence CBPL was not added in Model 1 for these sections.

We also tried BB plus a Comptonized emission (hereafter **Model 2**). We used the *nthComp* component in XSPEC (see Zdziarski, Johnson, and Magdziarz 1996 for details) to describe the Comptonized emission. Finally, we attempted a combination of MCD and *nthComp* (hereafter **Model 3**) components to describe the X-ray spectra of this source. Both models have been widely used to fit the spectra of the NS-LMXBs (Di Salvo et al. 2001; Barret 2001; Di Salvo et al. 2002; Agrawal and Sreekumar 2003; Agrawal, Nandi, and Katoch 2023). We also need an additional smeared edge component (at  $\sim 7-8$  keV) to improve the fit. **Model 2** does not require this additional smeared edge component. *TBabs* model (Wilms, Allen, and McCray 2000) is used to take into account the absorption of X-rays in the inter stellar medium. We added 2 per cent systematic error while carrying out the joint spectral fitting of the *LAXPC20* and *SXT* spectra in XSPEC to account for uncertainty in the response matrices of both detectors. We also added a multiplicative constant component to account for the cross calibration related uncertainties. We take shape of the seed photon spectrum as blackbody while fitting the data with **Model 3** and *diskbb* for **Model 2**.

We also attempt to fit the data with *Comptb* model, which takes care of both thermal and bulk Comptonization (Farinelli et al. 2008). This models is sum of two components, the soft seed photons which has not undergone up-scattering and coming directly and the component that is Comptonized. We fix  $\gamma = 3$  (blackbody seed photon). We find that parameter  $\log A$  pegs to 8 and  $\delta \ll 1$ . Since seed photons from disc can also be Comptonized by the Corona, we included one more *Comptb* component and tied the value of spectral index  $\alpha$  and electron temperature  $kT_e$  while fitting the data with double *Comptb*. For the second *Comptb* component  $\log A$  pegs to -8 and  $\delta \ll 1$ . For the first *Comptb* component, illumination factor ( $A/(A+1)$ ) is close to one and for the second *Comptb* component it is negligible. Hence, we reached to conclusion that the bulk Comptonization is not present, disk photons are seen directly and blackbody photons from the NS surface is completely Comptonized. Hence, we fit the data with *Comptb* plus *diskbb* component (**Model 4**) which allow us to calculate the inner disk radius as well. We have shown the unfolded spectra using **Model 4** for the segments, HB1, HB3, NB1, NB4 and FB2 for a comparison in Figure 5. We compared Model-4, with Model-1 and Model-2 by computing F-test chance improvement probabilities for addition of extra parameters. **Model 3** and **Model 4** has similar reduced  $\chi^2$ . **Model 4** provides statistically better fit compared to **Model 1** and **Model 2** (see Table 6). We also note that **Model 2** does not constrain the seed photon temperature in the segments HB3-FB2. The `cfIux` command is used to derive the unabsorbed fluxes in the individual spectral components. The disk and Comptonization fluxes are computed in the energy range 0.5–50.0 keV. Errors quoted in the best fit parameters are 1- $\sigma$  errors and computed using  $\Delta\chi^2 = 1$ .

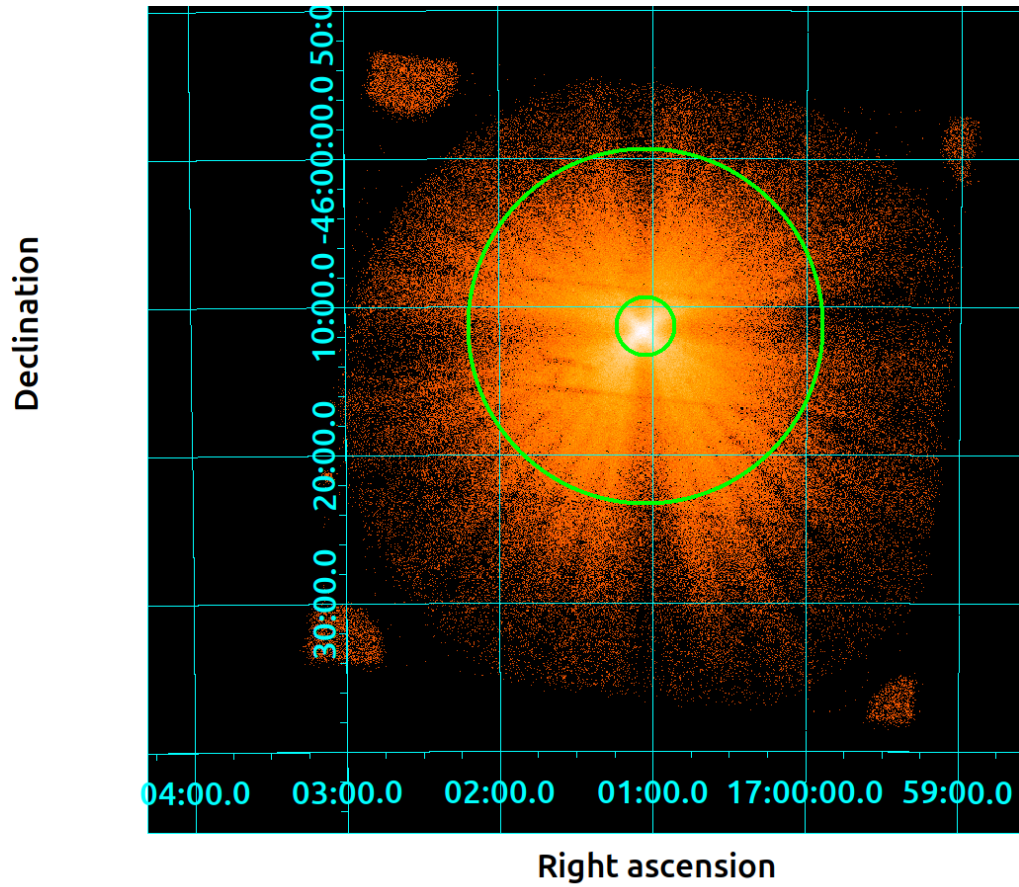


**Figure 1.** The figure shows the *SXT* image of the source in the 0.3 – 8 keV energy band. The bright spots at the four corners are image of Fe<sup>55</sup> calibration sources. The annular region used to extract the lightcurves and spectra is also shown. For details see the text.

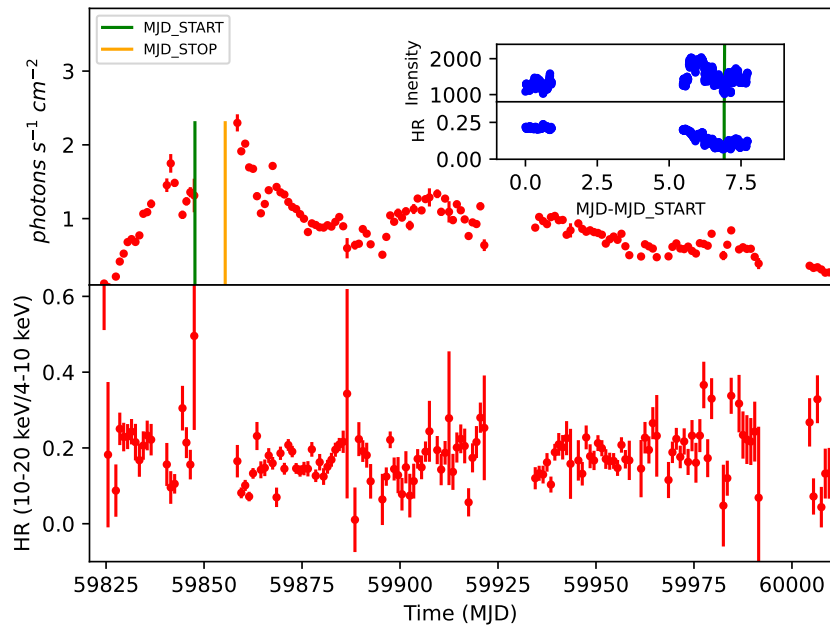


**Figure 2.** The figure shows the *MAXI* lightcurve of the source in the energy band 2 – 20 keV and hardness ratio calculated using energy band 10-20 keV and 4-10 keV. The two vertical line marks the *AstroSat* observations. The inset figure in top panel shows the LAXPC lightcurve in 3 – 60 keV energy band and hardness ratio calculated using energy bands 9.7-20 keV and 4.6-9.7 keV. In the inset figure intensity is defined as counts rate in the 3-60 keV energy band. The start and stop time of the dipping FB is marked by two vertical lines in the inset figure. Since the dip period is short ( $\sim 3000$  seconds) both vertical lines are merged.

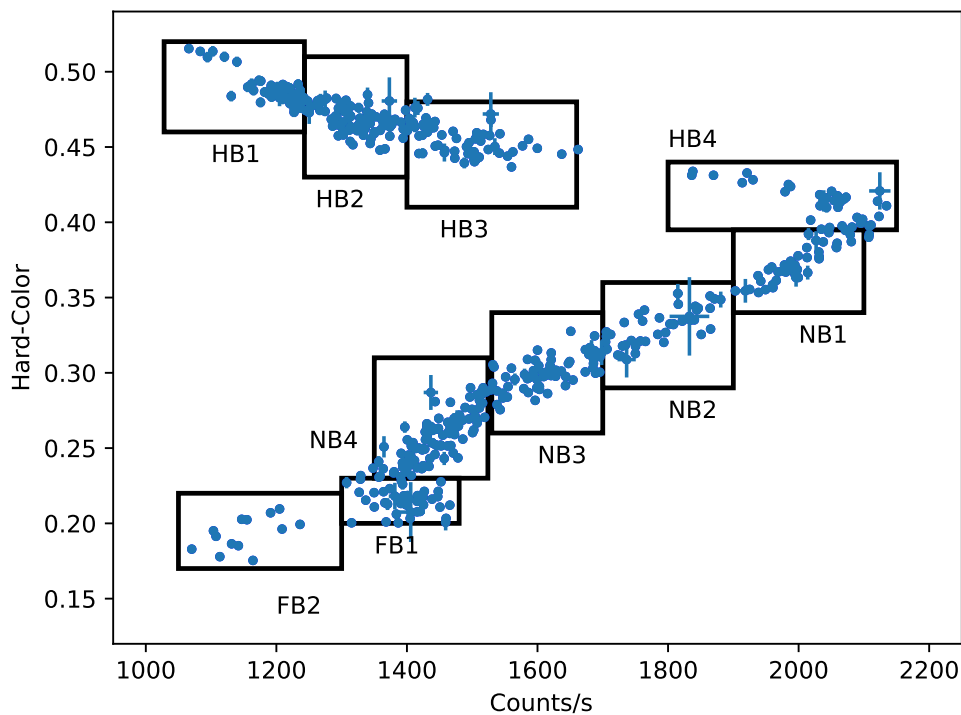


**Figure 3.** The figure shows the HID of the source. Hard-color is ratio of the count rates in the energy bands 9.7 – 20 keV and 6.5 – 9.7 keV and intensity is defined as count rate in the energy range 3 – 20 keV.

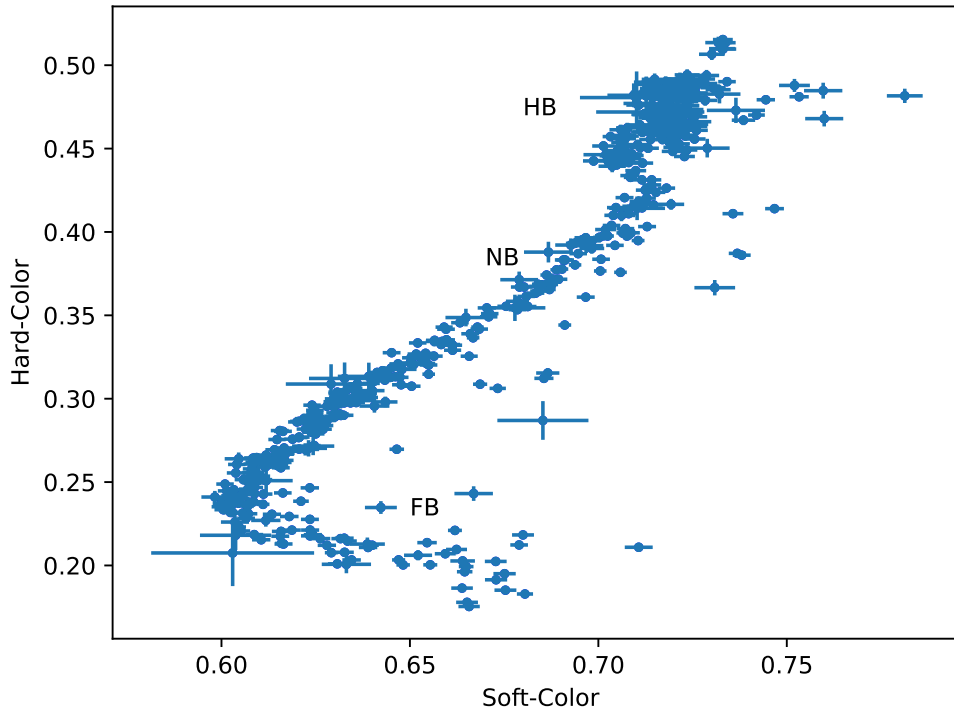


**Figure 4.** The figure shows the CCD of the source. Hard-color is ratio of the count rates in the energy bands 9.7 – 20 keV and 6.5 – 9.7 keV and soft color is defined as count rate in the energy range 4.6 – 6.5 and 3.0 – 4.6 keV.

### 3.3 Timing Analysis

We carry out fast timing analysis using the *LAXPC20* data. Using the *LAXPC20* data, we generated 2-ms binned lightcurves in the energy band 3 – 50 keV for each data points (with 256s length) of HID. We divided these lightcurves in intervals of 4096 bins and created the PDS for these intervals. This procedure produces PDS in the frequency range 0.12 – 250 Hz for each intervals. PDS belonging to same segments of the HID were averaged and re-binned geometrically by a factor of 1.03 in the frequency space. The PDS were normalized to give fractional root-mean squared power  $((rms/mean)^2/Hz)$  and dead time corrected Poisson noise was subtracted (Zhang *et al.* 1995; Agrawal *et al.* 2018). We performed the fitting of PDS in the frequency range 0.12 – 250 Hz using the combination of Lorentzian and power-law components. The Lorentzian function is defined as

$$\frac{r^2 \Delta\nu}{2\pi[(\Delta\nu/2)^2 + (\nu - \nu_c)^2]}, \quad (1)$$

where  $\Delta\nu$  is the full-width at half maxima (FWHM),  $\nu_c$  is the centroid frequency and  $r$  is the integrated rms for the Lorentzian component (Belloni, Psaltis, and van der Klis 2002). 1- $\sigma$  errors (68% confidence) in the best fit parameters are calculated using  $\Delta\chi^2 = 1$ . We also created PDS in the energy bands 3–5 keV, 5–8 keV and 8–15 keV to carry out the energy dependent study of the observed power-spectral features.

## 4. Results

### 4.1 Spectral Nature of XTE J1701-462

In Figure 3, we show the HID of the source. The HID has an extended HB and short and dipping FB. Figure 4 shows the CCD of the source. The points belonging to the HB on the CCD are clustered. The source traced similar pattern on the CCD and HID during the Cyg-like phase of 2007 outburst (Homan *et al.* 2007). We fit the broad band X-ray spectra corresponding to different segments of the HID of the source using various popular spectral models and study evolution of the parameters along the Z-track. We note that both **Model 4** and **Model 3** comprising disk-blackbody and Comptonized emission are statistically better description of the data. The seed photon energy can not be constrained for sections HB3 to FB2, while using **Model 2**. It is also noted that the high blackbody temperature ( $\sim 3$  keV) obtained by fitting the broad band spectra with **Model 1** seems to be unphysical. In Figure 5 we show the unfolded X-ray spectra for different sections fitted with **Model 4**. The best fit parameters obtained using **Model 1**, **Model 2**, **Model 3** and **Model 4** are listed in Table 1, Table 2, Table 3 and Table 4 respectively. The unabsorbed disk and Comptonized component fluxes are listed Table 5. The model component *diskbb* has two parameters, the inner disk temperature  $kT_{in}$  and the normalization  $K$ . The normalization

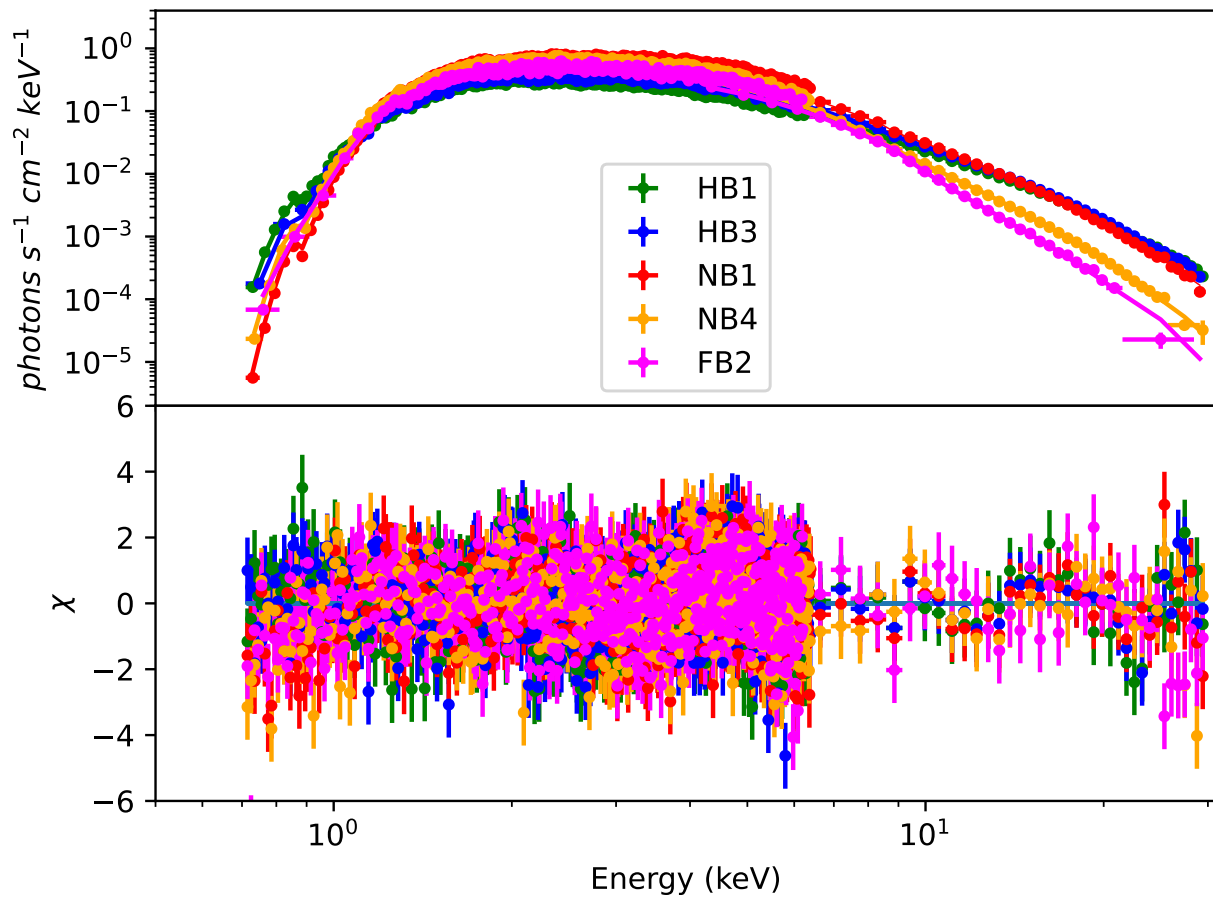


**Figure 5.** In the top panel of the figure the unfolded spectra and the best fit model together for the segments HB1, HB3, NB1, NB4 and FB2 have been plotted. The best fit model used here is  $tbabs*(diskbb+Comptb)$ . The residual in units of sigma for these segments is also plotted in the bottom panel of the figure.

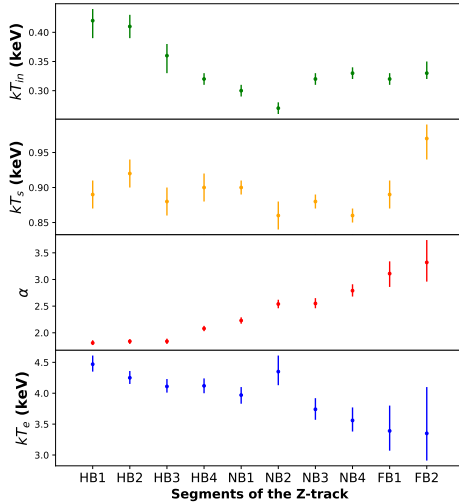


**Figure 6.** Figure shows evolution of the parameters of **Model 4** ( $tbabs^*(Comptb+diskbb)$ ). The electron temperature  $kT_e$  and spectral index  $\alpha$  show significant evolution as the source moves from HB to FB. The Comptonized component becomes softer from segment HB1 to FB2. Also disk temperature decreases as the source moves from the segment HB1 to NB2. For details see the text and Table 4.

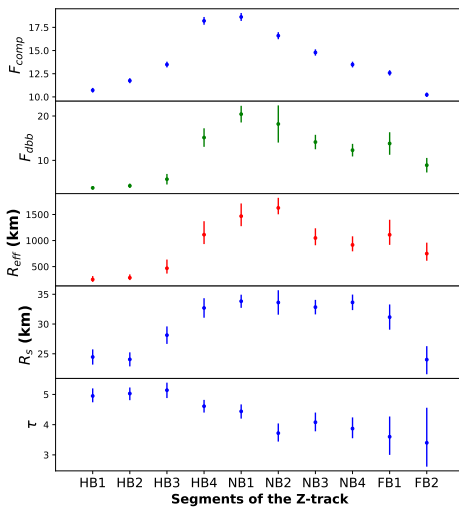


**Figure 7.** Figure shows evolution of the Comptonized ( $F_{Comp}$ ) flux, disk flux ( $F_{dbb}$ ), the effective inner disk radius ( $R_{eff}$ ) and the optical depth ( $\tau$ ) of the corona, calculated for **Model 4**. Significant evolution of the disk and the Comptonized flux is clearly visible. The effective disk radius and optical depth ( $\tau$ ) also evolve significantly from the segment HB1 to FB2. For details see the text and Table 5.

$K$  is connected with the inner disk radius  $R_{in}$  by the relation,

$$K = \left( \frac{R_{in}}{D_{10}} \right)^2 \cos \theta, \quad (2)$$

where  $D_{10}$  is the distance in units of 10 kpc and  $\theta$  is inclination angle of the disk (Mitsuda et al. 1984). We assumed distance of the source to be 8.8 kpc and inclination angle to be  $60^\circ$  (Lin et al. 2009; Lin, Remillard, and Homan 2009). The absence of iron line (as in the present case) or presence of weak iron line and absence of X-ray dips and eclipses suggests that inclination should be less than  $70^\circ$ . Hence, we chose an average inclination angle of  $60^\circ$  to compute the inner disk radius. The local blackbody spectrum from the accretion disc is modified by scattering processes and can be best represented by a diluted blackbody (Shimura and Takahara 1995) given by equation

$$F_{\nu}^{db} = \frac{1}{f^4} \pi B_{\nu}(f T_{eff}), \quad (3)$$

where  $f$  is spectral hardening factor,  $T_{eff}$  is effective temperature. The effective temperature is given by  $T_{eff} = \frac{T_{in}}{f}$  and effective inner accretion on disc radius is given by  $R_{eff} = f^2 R_{in}$ . We computed the color correction factor  $f$  using the equation (Davis and El-Abd 2019)

$$f \approx 1.48 + 0.33(\log \dot{m} + 1) + 0.07(\log \alpha + 1) + 0.02(\log(M/M_{\odot}) - 1), \quad (4)$$

here  $\dot{m}$  is the mass accretion rate in unit of Eddington rate,  $\alpha$  is the viscosity parameter and  $M$  is the mass of neutron star. Color factors are listed in Table 5.  $R_{eff}$  was derived using these values and given in the Table 5. The *Comptb* component has four free parameters, the spectral index  $\alpha$ , the electron temperature  $kT_e$  of the hot corona, the seed photon energy  $kT_s$ , and the normalization. The radius of seed photon emitting region is given by the equation (see in 't Zand et al. 1999),

$$R_s = 3 \times 10^4 \sqrt{F_{Comp}/(1 + \gamma)/(kT_s)^2} \quad (5)$$

The above equation is obtained by equating the soft seed photon luminosity with blackbody luminosity of temperature  $kT_s$  where  $\gamma$  is the Compton  $\gamma$ -parameter that gives relative energy gain due to Compton scattering and is given by the relation

$$\gamma = \frac{4kT_e}{m_e c^2} \tau^2, \quad (6)$$

where  $\tau$  is the optical depth.

The spectral index of Comptonized component is given by (see Zdziarski, Johnson, and Magdziarz 1996)

$$\alpha = \left[ \frac{9}{4} + \frac{1}{kT_e/m_e c^2 (1 + \tau/3)} \right]^{1/2} - \frac{3}{2} \quad (7)$$

We solve this relation for optical depth  $\tau$ . The optical depth depends upon  $\alpha$  and electron temperature  $kT_e$ . We show the variation of the fitted (see Figure 6) and derived parameters

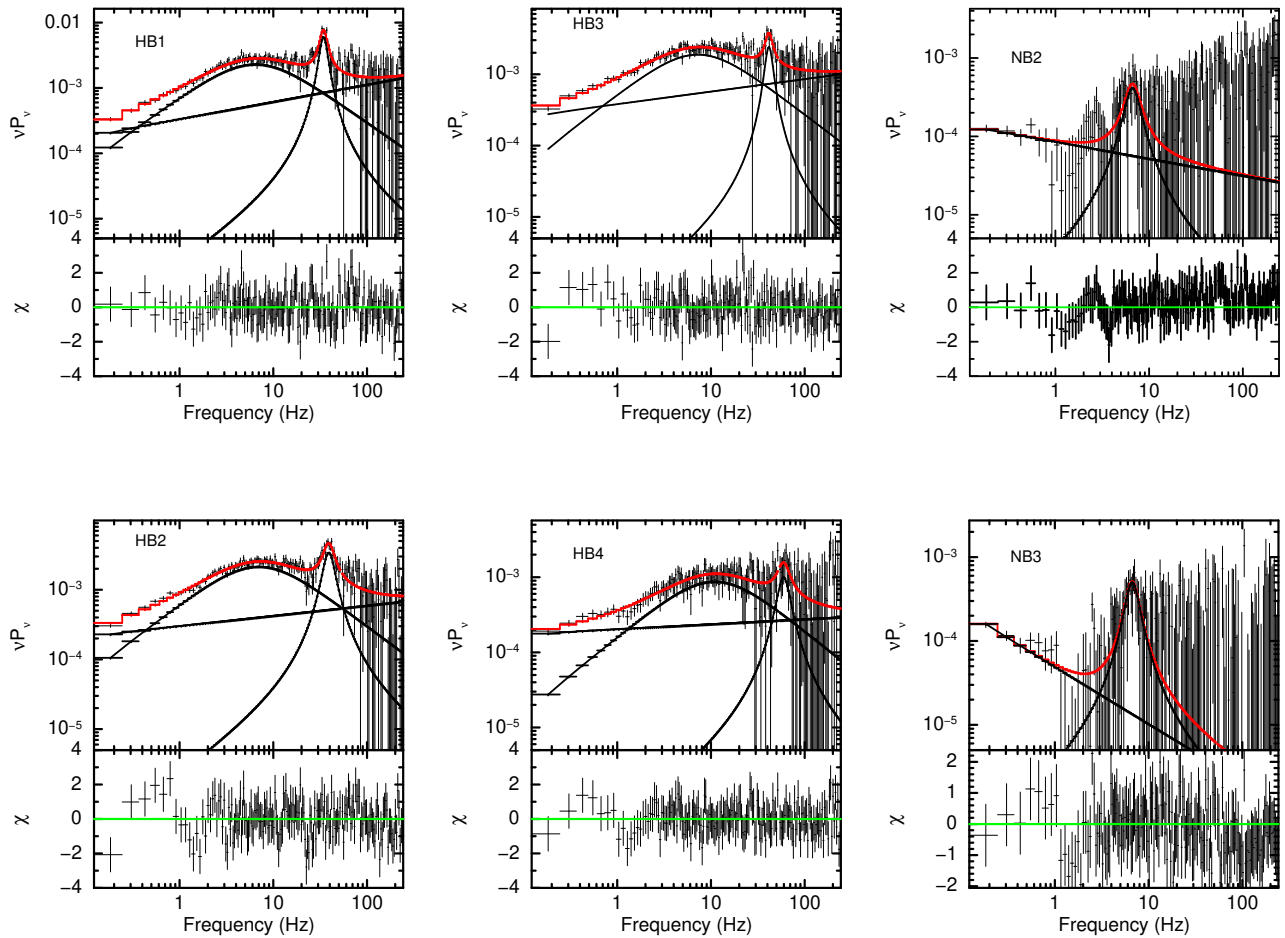


**Figure 8.** Figure shows the PDS for HID segments HB1, HB2, HB3 HB4, NB2 and NB3 in the energy band 3 – 50 keV. In HB1, HB2 and HB3, a HFO is detected. A NBO is seen in the NB2 and NB3. The PDS for segments HB1, HB2 and HB3 are fitted with the combination of double Lorentzian and a power-law. The PDS for segments NB2 and NB3 are fitted with the combination of a power-law and a Lorentzian. Best fit model along with the observed PDS has been shown in the figure.

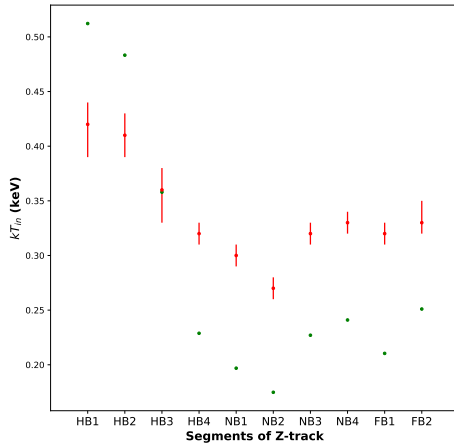


**Figure 9.** A comparison between the observed inner disk temperature and derived values. The estimated temperature values are denoted using green dots and the fitted values are shown using red dots with error.

(Figure 7) of **Model 4** as a function of position on the HID. An increase in the  $\alpha$  from  $\sim 1.81$  to  $3.32$  is observed with the movement of the source from the HB to the NB then to the FB, suggesting that the Comptonized spectrum is becoming softer. The electron temperature  $kT_e$  of the Compton corona also decreases from  $4.48$  to  $3.35$  as the source moves along the Z-track from HB to FB. The seed photon temperature remains almost constant and remains in the narrow range  $0.9$ – $1.0$  keV. The disk temperature  $kT_{in}$  decreases from  $\sim 0.42$  to  $\sim 0.28$  keV from the segment HB1 to NB2 and then remains almost unchanged in the rest of the Z-track. Our analysis also reveals that the flux of the Comptonized emission in the energy range  $0.5$ – $50$  keV increases from HB1 to NB1 and then decreases from NB1 to FB2. The disk flux also show a variation similar to the Comptonized flux as the source moves along the HID. We also note that the inner disk radius  $R_{eff}$  changes from  $\sim 250$  km to  $\sim 1600$  km as as the source evolves from the state HB1 to NB2 and as it moves further from NB3 to FB2 the disk radius decrease to  $\sim 750$  km. The seed photon radius  $R_s$  is found to be in the range of  $\sim 25$ – $36$  km being lowest in the upper HB (HB1 and HB2). The optical depth  $\tau$  of the corona is slightly higher ( $\tau \sim 4.6$ – $5.1$ ) in the HB compared to that in NB and FB. A decrease in  $\tau$  from  $\sim 4.6$  to  $\sim 3.4$  is seen with the motion of the source from HB4 to FB2. The  $\gamma$ -*par* remains almost constant in HB and then decreases along the NB and FB (see Table 5).

#### 4.2 Timing behavior of XTE J1701-462

To describe the features in the PDS we need Lorentzian and power-law (Power  $\propto \nu^{-\alpha}$ ) components. The power-law function describes the very low frequency noise (VLFN). A zero centred Lorentzian describes the band limited noise (BLN). The narrow features observed in the PDS are also represented by a Lorentzian. Following Belloni, Psaltis, and van der Klis (2002), we define the characteristic frequency of the narrow

features (QPO) as,

$$\nu_{char} = \sqrt{(\Delta\nu/2)^2 + \nu_c^2}, \quad (8)$$

where  $\nu_c$  and  $\Delta\nu$  are centroid frequency and *FWHM* (see Equation 1). The break frequency of BLN component is given by  $\Delta\nu/2$ , where  $\Delta\nu$  is the FWHM of the zero centred Lorentzian component. The quality factor (Q) of the QPO is defined as  $\nu_c/\Delta\nu$ . The best fit parameters of power-spectral features are listed in the Table 7 and their rms values are given in Table 8. We detect narrow QPOs (HBOs) with  $\nu_{char}$  (or  $\nu_{HBO}$ ) in the range  $34$ – $40$  Hz in the HID segments HB1, HB2 and HB3 (see Figure 8 and Table 7). The significance of HBOs are  $12.7\sigma$ ,  $10.8\sigma$  and  $5.8\sigma$  for segments HB1, HB2 and HB3 respectively. We also detect a weak HBO-like feature in HB4 with significance  $2.6\sigma$ . The significance of QPOs is computed by taking ratio of the normalization of the Lorentzian and 1-sigma negative error on normalization (see Sreehari et al. 2020; Majumder et al. 2022). BLN feature with break frequency varying from  $\sim 6.5$  Hz to  $\sim 11$  Hz is seen in this region of HB (HB1–HB4). The frequency  $\nu_{HBO}$  and  $\nu_{break}$  increases as the source travels from HB1 to HB4. This suggest that the frequency of both components are correlated. NBOs with  $\nu_{char}$  (or  $\nu_{NBO}$ )  $\sim 6.7$  Hz with rms  $\sim 1.7\%$  is observed in the HID section NB2 and NB3 (see Figure 8). The significance of NBOs is given in the Table 7. The rms of the HBOs decreases from  $\sim 4.5\%$  to  $\sim 2.8\%$  as the source travels from HB1 to HB3. The rms of the BLN feature also shows a decrease from  $\sim 8.5\%$  to  $\sim 5.2\%$  from HB1 to HB4. The total rms in the PDS decreases as the source moves along the HID from HB1 to FB2. We also find a broad high frequency feature with a quality factor  $< 2$  with  $\nu_c \sim 59$  Hz in NB1. Since quality factor of this feature is small, we do not consider it as HBO. We also detect a low-frequency noise (LFN) with  $\nu_{char} \sim 9.6$  Hz in this section of NB.

We have also carried out energy dependent study of the power-spectral features (see Table 9 for details). The strength of the HBOs increases with increase in the energy of X-ray photons. This trend is observed in the HID sections HB1, HB2 and HB3. However, PDS created in the narrow energy ranges  $3$ – $5$  keV,  $5$ – $8$  keV and  $8$ – $15$  keV do not show a significant HBO for the HID segment HB4. Moreover, the rms of BLN feature also show increasing pattern with an increase in the energy. In HB3, HBO was found to be absent in the energy range  $3$ – $5$  keV and we set an upper limit of  $< 1.97\%$  on the rms of this feature.

#### 5. Discussion

As shown in Figure 3, both *AstroSat* observations are close to the peak of the 2022 outburst. During the *AstroSat* observations the source showed a Cyg-like behavior. Its HID has an extended HB, a short and dipping FB. The source count rate increases by a factor of two along the HB. A similar HID was observed in the source previously with *RXTE* near the peak of the 2006 outburst (Homan et al. 2007). The broad-band spectral data acquired with *SXT* and *LAXPC* were fitted with

the four widely accepted approaches as described in the section 3. The combination of emission from a standard accretion disk (Shakura and Sunyaev 1973; Mitsuda et al. 1984) and Comptonized emission from a hot corona (Zdziarski, Johnson, and Magdziarz 1996; Farinelli et al. 2008) provides a better description of the X-ray spectra of the source. We study the evolution of the parameters of this model along the HID. Previously, spectral evolution study along the HID of the source in the energy band 3 – 100 keV has been carried out using the *RXTE* data (Lin et al. 2009). Hence, this is the first study covering energy band 0.7 – 30 keV. The fast timing analysis revealed the presence of the HBOs (34 – 40 Hz) in the HB and the NBOs at frequency  $\sim 6.6$  Hz in the NB. We discuss the origin and nature of these features observed in the PDS.

The inner disk is truncated far away from the NS ( $R_{\text{eff}} \sim 250 - 1600$  km). Hence, the region between the inner disk rim and the magnetosphere is filled with hot coronal plasma. A large inner accretion disk radius ( $R_{\text{eff}}$ ) has been reported in the Z-sources GX 340+0 (Bhargava et al. 2023) and GX 5-1 (Shyam Prakash and Agrawal 2024). Bhargava et al. (2023) suggests that probably the inner accretion disk is hidden inside a large corona. Other possibility is that the disk may be truncated due to radiation pressure. In both cases, the corona is not compact instead it is extended covering the NS surface and magnetosphere. We also note that the temperature changes by a smaller factor compared to the variation in the disk radius. Using the equation (Shakura and Sunyaev 1973)

$$T_{\text{in}} = \left( \frac{3GM\dot{M}}{8\pi R_{\text{in}}^3 \sigma} \right)^{1/4}, \quad (9)$$

we estimated the inner disk temperature and compared with observed temperature of the disk (see Figure 9). In this equation  $M$  is mass of the NS,  $\dot{M}$  is mass accretion rate. From Figure 9, it can be seen that the trend of change in the estimated values of  $kT_{\text{in}}$  and the fitted values of  $kT_{\text{in}}$  along the Z-track is similar. However, the the estimated and observed temperatures do not exactly match, suggesting that the nature of accretion disk may deviate from the standard accretion disk (Shakura and Sunyaev 1973) at high luminosities. The spectral modeling of emission from the source with *tbabs\*(diskbb+Comptb)* favor a truncated disk scenario. The disk flow probably starts deviating from Keplerian to sub-Keplerian flow at the inner edge to satisfy the inner boundary conditions at the NS surface. The transition from a Keplerian to a sub-Keplerian flow creates centrifugal barrier (CB) at the transition point where matter starts piling up vertically forming a transition layer (TL) (Chakrabarti and Titarchuk 1995; Chakrabarti 1997; Titarchuk, Lapidus, and Muslimov 1998). The soft photons from the NS surface is up-scattered by the hot electrons present in the TL (Farinelli et al. 2008). The small illumination factor ( $A \ll 1$ ) for second Comptb suggests that emission from the disk is seen directly. Hence, the transition layer is geometrically thick and located between inner edge of accretion disk (which is truncated) and the NS magnetosphere. The photons from the NS are completely hidden and intercepted by an

optically thick ( $\tau \sim 3 - 5$ ) and geometrically thick TL. The bulk flow parameter  $\delta$  is zero, suggesting that the bulk flow is suppressed due to the strong radiation pressure at the vicinity of the NS. The bolometric unabsorbed luminosity in the energy range 0.5 – 50 keV of the source increases along the HB becoming highest at the hard apex and then again decreases along the Z-track. The disk and Comptonized luminosity follow a similar trend. Based on the multi-frequency observations of Cyg X-2, Hasinger et al. (1990) argued that accretion rate monotonically increases from HB to NB and then FB. However, opposite scenario has also been proposed to explain the ‘Z’ tracks of Cyg-like Z-sources (Bałucińska-Church et al. 2011). The Comptonization flux show a systematic increase from HB1 to NB1. The location of inner edge of the disk is decided by balance between ram pressure and radiation pressure of Comptonized flux. The corona can be considered as a transition layer between inner edge of accretion disk and  $R_{\text{ISCO}}$ . An increase in the radiation pressure or radiation drag may push the disk outwards. Indeed, the inner disk radius also increases from HB1 to NB1. The electron temperature of the corona shows slight decrease (4.47 to 3.97) and the optical depth does not show much variations from HB1 to NB1. However, the Comptonization flux increases due to increase in its normalization. Since the inner rim of the disk and outer edge of the TL is moving outwards, size of the corona increases. This suggests that the corona should become optically thin and hot as the source travels along the HB. The increase in the soft seed photon luminosity reverse this expected change in the corona and also explains the observed brightening of the corona from HB1 to NB1.

The reduction of coronal luminosity is observed from NB1 to FB2. Also, we note that the spectra become softer (or hard color decreases) and count rate decreases along this section of HID. The change in the hardness ratio is basically decided by the variation in the Comptonized component. The electron temperature decreases slightly (4.3 – 3.3 keV) and the optical depth shows slight decrease (4.4 to 3.4) from the segment NB1 to FB2. The Sco-like Z-source GX 17+2 has also shown similar behavior in the NB (Agrawal, Nandi, and Ramadevi 2020). In GX 17+2, the optical depth decreases and electron temperature remains almost constant along the NB. It was proposed that an increase in the seed photon supply from the boundary-layer or the NS surface causes a small fraction of coronal material to cool down and settle down in an underlying accretion disk. This mechanism leaves slightly less denser plasma cloud, explaining observed decrease in the optical depth along the NB. However, in the present case we note that the soft seed photons from the NS surface decreases along the NB and FB. The decrease in the luminosity with an increase in the mass accretion rate can be explained by increase in anisotropy of the X-ray emitting region causing decrease in the fraction of the X-ray flux emitted towards the observer’s line of sight. Most probably the height ( $H$ ) of the corona is increasing and at the same time its shape is changing from TL with  $H/R_{\text{in}} < 1$  to slightly asymmetric flow with  $H/R_{\text{in}} \sim 1$ . This may explain the decrease in the optical depth (as volume of the corona increases and hence density decreases). The increased

supply of seed photons from the NS surface, anticipated due to increase in accretion rate can cause decrease in the coronal temperature from NB1 to FB2. A decrease in the polarization degree (PD) has been observed as the source moves HB to NB. The decrease in the scattering efficiency of the corona from from the hard apex to the lower NB can explain the observed decrease in the PD.

We observe a dipping FB in this source, such a dipping behavior has been observed in Z-sources, GX 340+0 (Peter G. Jonker et al. 1998), GX 5-1 (Wijnands et al. 1998) and Cyg X-2 (Mondal et al. 2018). This source also has shown a dipping FB during its previous outburst (Homan et al. 2007). The dipping FB in the source is associated with a reduced optical depth and a lower coronal temperature. This is opposite to behavior observed in Cyg X-2 where the optical depth was found to increase during the X-ray dips (Mondal et al. 2018). Multi-wavelength study of Cyg X-2 suggested that the X-ray dip is caused by absorption of an extended coronal emission by the structure in the outer accretion disk (Bałucińska-Church et al. 2011). Hence, changing corona geometry (X-ray emitting region becomes anisotropic in the FB) can explain the X-ray dips observed in the source.

This source has shown, HBOs, NBOs and a pair of kHz QPOs during the previous outburst (Homan et al. 2007). The source exhibited kHz QPO pairs in Z-phase and single kHz QPO in atoll-phase (Sanna et al. 2010). In the Z-phase, kHz QPOs were weaker and broader compared to the atoll-phase. The timing properties of the source was studied in detail during the Cyg-like phase (Homan et al. 2007) where the source exhibited dipping FB. It was noted that frequency of HBO increases and rms strength decreases along the HB. During *AstroSat* observation also the source was in Cyg-like phase and showed dipping FB, suggesting that temporal and spectral properties of the source should be similar. During the *AstroSat* observations the source exhibited HBOs in the frequency range 34–40 Hz. The strength of the HBOs observed in the source decreases as the source travels from HB1 to HB3 and then they disappear as the source further moves down the Z-track. The Comptonization flux increases from HB1 to HB4. However ratio of the Comptonization flux and total flux decreases along the HB and hence the HBO rms is correlated with the percentage contribution of Comptonized emission to the total flux. Bu et al. (2015) investigated the HBO properties of the source using all available *RXTE* observations of the source during its 2006 outburst. They also found that the HBO rms decreases from top-left of the HB to the hard-apex. The rms of the HBOs and the BLN component increases with increase in the photon energy from 4 to 12 keV (see Table 7). Energy dependent studies of HBOs of this source using data from *RXTE* satellite also provided a similar result in this source (Bu et al. 2015). GX 340+0 also shows increase in the HBO strength with increasing photon energy (Peter G. Jonker et al. 2000). Hard nature of the HBOs and the BLN component suggests that their origin is linked with the hot corona around the compact object. We find a positive correlation between the break frequency and the HBO frequency, consistent with the previous observation of the source (Bu et al. 2015). Moreover,

frequency resolved spectroscopy of the HBOs suggests that these oscillations are produced in the Comptonizing region (Revnivtsev and Gilfanov 2006).

In many models of QPOs, the kHz QPOs and HBOs are linked with the inner disk radius (Miller, Lamb, and Psaltis 1998; Stella and Vietri 1999). According to these models the upper kHz QPOs depends upon the location of inner edge of accretion disk. The observed kHz QPOs (Sanna et al. 2010) in the XTE J1701-462 gives  $R_{in} \sim 20$  km. In the present case, disk is truncated away from the NS surface. If spectral nature of the source during the Z-phase of the previous outburst and the present outburst are similar then the origin of kHz QPOs can not be explained in the framework of these QPO models. Presently, we have detected only HBOs and NBOs in the Cyg-like Z-phase of the source.

The Lense-Thirring (LT) precession model has been proposed to explain the HBOs observed in NS-LMXBs and LFQPOs in black hole binaries (Ingram, Done, and Fragile 2009). According to this model precession of radially extended hot central corona produces the observed QPOs in these two class of objects. The outer radius of the hot flow is decided by the truncation radius of the disk. The disk is truncated  $\sim 250$ –1100 km in the segments HB1 to HB4 sections of the Z-track. We take outer radius  $r_o = R_{eff}/R_g$  and inner radius  $r_i = R_{NS}/R_g$  of the hot radial flow. The LT precession frequency is computed using the formula (Ingram, Done, and Fragile 2009)

$$\nu_p = \frac{5}{\pi} \frac{a[1 - (r_i/r_o)^{1/2}]}{r_o^{5/2} r_i^{1/2} [1 - (r_i/r_o)^{5/2}]} \frac{c}{R_g}, \quad (10)$$

where  $R_g = 2.1$  km is gravitational radius of  $1.4 M_\odot$  neutron star.  $R_{NS} = 10$  km is NS radius. The above equation gives the QPO frequency of 0.2 Hz for  $R_{eff} = 250$  km. Hence, this model can not explain the origin of the HBOs observed in the NS-LMXBs. Li et al. (2014) observed a positive correlation between the inner disk radius and the HBO frequency. We also observed a similar correlation, which is hard to explain in the framework of the LT precession model. **Probably**, the LT precesses differentially with a higher precession frequency at the inner region of TL compared to outer region (van den Eijnden, Ingram, and Uttley 2016; Huang et al. 2018). Here, we can assume that TL is slightly warped where height of TL is higher in the inner region compared to that in outer region. Hence more modulation is produced by the faster precessing inner region.

Recently phase resolved polarimetry of a strong LFQPOs, seen in the transient blackhole candidate Swift J1727.8-1613, has been carried out (Zhao et al. 2024). No modulation in the polarization degree and the polarization angle is observed with the QPO phase. Hence polarimetric observations are also not in favor of the LT precession model. LT precession model of jet and inner disk ring has been used to explain the LFQPOs seen in Swift J1727.8-1613 (Yu, Bu, Zhang, et al. 2024). LFQPO in the hard X-rays was detected in Swift J1727.8-1613 with *AstroSat* (Nandi et al. 2024). It was suggested that the oscillations in a hot and dense downstream flow at the vicinity of the blackhole produces the QPOs (Nandi et al. 2024).

IGR 17480-2446, which is a transient milli-second pulsars with 11 Hz pulse period, exhibited HBOs (35 – 50 Hz) and kHz QPOs (Barret 2012; Altamirano et al. 2012). This source also showed transition from atoll to luminous Z-phase (Chakraborty, Bhattacharyya, and Mukherjee 2011). To explain the nature of HBO in this source the Altamirano et al. (2012) suggested that precession due to frame dragging alone is not sufficient to explain the observed frequency of HBOs. They proposed that a warp is induced by magnetic field in the hot inner flow and that precesses with frequency  $\nu_{mag}$ . The magnetic precession depends on the magnetic moment  $\mu$ . The net precession frequency is combination of magnetic and frame dragging effects.

As HBOs are linked to the Comptonizing component, other kind of oscillations in the corona can produce these frequencies. Cabanac et al. (2010) proposed the oscillating hot corona model to explain the low frequency QPOs seen in X-ray binaries. They suggested that a magneto-acoustic wave propagating in the hot corona can produce resonant peaks in the PDS.

Another popular model proposed to explain the origin of the QPOs is two-oscillator model (Osherovich and Titarchuk 1999). According to this model hot, large and inhomogeneous blobs are formed at the outer edge of the TL and injected into the NS magnetosphere. If the blobs formed at the outer edge of the TL are rotating differentially, having higher angular velocity at inner edge compared to outer edge. These blobs with certain velocity distributions are injected to the NS magnetosphere from the inner edge of TL. Such blobs under influence of Coriolis force behave as Keplerian oscillators with two modes : radial and vertical (Osherovich and Titarchuk 1999). The radial mode is identified with upper kHz QPO and the mode perpendicular to the accretion disk produces the HBOs. The lower kHz QPO is identified with the Keplerian frequency of the blobs at the inner edge of TL. These hot plasma balls intercept the photons from the NS surface and up-scatter them. Hence, we expect rms strength of the HBOs to be positively correlated with the energy of photons. A positive correlation seen between the HBO-rms and the photon energy support this scenario. The radiation pressure increases as the source moves from HB1 to HB4 due to increase in the source luminosity. The increasing radiation pressure disrupts the flow of hot blobs responsible for HBOs. Therefore, HBOs become weaker as the source moves down the HB and disappear as source moves further along the Z-track. The observed LFQPOs (HBOs and NBOs) can also be explained in the framework of oscillating shock wave model (Molteni, Sponholz, and Chakrabarti 1996). In this model, shock oscillates radially with a time period equal to the cooling time scale of the corona. NBOs at frequency  $\sim 6.6$  Hz are seen in the middle and lower NB. The frequency of NBOs always lies in the narrow range ( $\sim 5 - 7$  Hz), suggesting that they are linked with some kind of fundamental frequency of accretion flow close to the NS (Hasinger 1987). According model proposed by Hasinger (1987), at high accretion rate the inhomogeneous plasma is accreted at the free fall velocity and causes density fluctuations in a layer above the NS surface.

The density fluctuations propagates with local sound speed on the NS surface given by

$$\nu_s = 4.2 \times 10^7 R_6^{-1/4} \left( \frac{M}{M_\odot} \times \frac{L}{L_{Edd}} \right), \text{ cm s}^{-1} \quad (11)$$

where  $R_6$  is NS radius in units of  $10^6$  cm (Hasinger 1987). The propagation of these fluctuations on the NS surface produces NBOs. Due to variations in mass accretion rate, a spectrum of density fluctuations will be produced, the fundamental tone of which is given by

$$\nu_s = \frac{v_s}{2\pi R} \text{ Hz}, \quad (12)$$

where  $R$  is the neutron star radius. It is clear that the  $\nu_s$  depends upon the NS radius, mass accretion rate (which is always close to Eddington limit for 1.4 solar mass NS) and mass of the NS (Hasinger 1987). Therefore, the NBO frequency lies in a narrow range around 6 Hz. Alternatively, it can be produced by acoustic oscillations of a spherical shell around the NS (Titarchuk et al. 2001). In this scenario, transition layer can become spherical at high accretion rate. The spherical shell oscillates with a frequency,

$$\nu_s = \frac{f v_s}{L} \text{ Hz}, \quad (13)$$

where,  $f=0.5$  or  $1/2\pi$ , depending upon the boundary conditions and  $L$  is size of the spherical shell. In this model of NBO, the oscillation frequency depends upon size of the spherical shell which can vary from source to source and hence suffers difficulties. Alternatively the observed NBOs can also be explained in the framework of oscillating corona model (Cabanac et al. 2010).

### Acknowledgement

Author thanks GH, SAG; DD, PDMSA, and Director URSC for encouragement and continuous support to carry out this research. Author thanks anonymous reviewer for useful and constructive suggestions which helped to improve the quality of the manuscript. This work has used the data from the LAXPC Instruments developed at TIFR, Mumbai and the LAXPC POC at TIFR is thanked for verifying and releasing the data via the ISSDC data archive. We thank the AstroSat Science Support Cell hosted by IUCAA and TIFR for providing the LaxpcSoft software which we used for LAXPC data analysis. This work has used the data from the Soft X-ray Telescope (SXT) developed at TIFR, Mumbai, and the SXT POC at TIFR is thanked for verifying and releasing the data and providing the necessary software tools.

**Data Availability Statement** Data underlying this article are available at AstroSat-ISSDC website <https://www.astrobrowse.issdc.gov.in/astroarchive/archive>.

**Table 1.** Best fit parameters obtained by fitting the spectra for all segments of HID using model  $tbabs^*(bbodyrad+diskbb)$  (Model 1). The fit parameters are  $N_H$  in units of  $10^{22} \text{ cm}^{-2}$ , disk temperature  $kT_{in}$ , disk normalization  $N_{MCD}$ , blackbody temperature  $kT_{BB}$  and blackbody normalization  $N_{BB}$ . The reduced  $\chi^2$  ( $\chi^2/dof$ ) is also given in the last column.

HID-Sections		Best fit parameters				
–	$N_H$	$kT_{in}$ (keV)	$N_{MCD}$	$kT_{BB}$ (keV)	$N_{BB}$	$\chi^2/dof$
HB1	$1.71^{+0.06}_{-0.06}$	$1.84^{+0.03}_{-0.04}$	$46.12^{+3.80}_{-4.27}$	$2.96^{+0.11}_{-0.11}$	$2.84^{+0.75}_{-0.51}$	686/633
HB2	$1.73^{+0.05}_{-0.07}$	$1.89^{+0.04}_{-0.05}$	$47.54^{+4.15}_{-5.17}$	$2.94^{+0.11}_{-0.12}$	$3.41^{+0.98}_{-0.69}$	697/633
HB3	$1.79^{+0.02}_{-0.02}$	$1.92^{+0.04}_{-0.04}$	$51.61^{+4.65}_{-4.12}$	$3.03^{+0.11}_{-0.11}$	$2.75^{+0.89}_{-0.60}$	720/633
HB4	$2.10^{+0.02}_{-0.02}$	$1.95^{+0.04}_{-0.04}$	$73.92^{+5.75}_{-5.33}$	$3.22^{+0.06}_{-0.05}$	$2.12^{+0.35}_{-0.29}$	754/634
NB1	$2.08^{+0.02}_{-0.02}$	$1.92^{+0.02}_{-0.02}$	$80.63^{+4.28}_{-4.10}$	$3.11^{+0.07}_{-0.06}$	$2.06^{+0.38}_{-0.31}$	930/634
NB2	$2.07^{+0.03}_{-0.02}$	$1.78^{+0.02}_{-0.02}$	$99.28^{+6.54}_{-6.01}$	$3.00^{+0.06}_{-0.06}$	$1.80^{+0.27}_{-0.23}$	810/634
NB3	$2.01^{+0.02}_{-0.02}$	$1.71^{+0.02}_{-0.02}$	$109.48^{+6.15}_{-5.72}$	$2.76^{+0.06}_{-0.06}$	$2.29^{+0.53}_{-0.35}$	821/634
NB4	$2.00^{+0.02}_{-0.02}$	$1.59^{+0.02}_{-0.02}$	$139.34^{+7.36}_{-6.88}$	$2.58^{+0.06}_{-0.05}$	$2.49^{+0.68}_{-0.51}$	814/634
FB1	$2.07^{+0.03}_{-0.02}$	$1.61^{+0.03}_{-0.02}$	$135.05^{+8.87}_{-9.55}$	$2.64^{+0.12}_{-0.08}$	$1.30^{+0.39}_{-0.25}$	725/634
FB2	$2.02^{+0.02}_{-0.02}$	$1.70^{+0.01}_{-0.02}$	$83.54^{+5.75}_{-5.35}$	$2.64^{+0.09}_{-0.13}$	$0.98^{+0.64}_{-0.37}$	837/634

**Table 2.** Best fit parameters obtained by fitting the spectra for different segments of HID using model  $tbabs^*(bbodyrad+nthComp)$  (Model 2). The fit parameters are the hydrogen column density  $N_H$  in units of  $10^{22} \text{ cm}^{-2}$ , the photon index  $\Gamma$ , the electron temperature  $kT_e$ , the seed photon temperature  $kT_s$  and normalization of the Comptonized component  $N_{COMP}$  the blackbody temperature  $kT_{BB}$  and the blackbody normalization  $N_{BB}$ . The reduced  $\chi^2$  ( $\chi^2/dof$ ) is also presented in the last column of the table.

HID-Sections		Best fit parameters						
–	$N_H$	$\Gamma$	$kT_e$ (keV)	$kT_s$ (keV)	$N_{COMP}$	$kT_{bb}$ (keV)	$N_{BB}$	$\chi^2/dof$
HB1	$1.85^{+0.07}_{-0.07}$	$1.98^{+0.02}_{-0.01}$	$3.74^{+0.04}_{-0.03}$	$0.31^{+0.10}_{-0.08}$	$1.81^{+0.39}_{-0.24}$	$1.21^{+0.02}_{-0.01}$	$194.35^{+11.66}_{-15.02}$	696/634
HB2	$1.93^{+0.06}_{-0.05}$	$1.98^{+0.02}_{-0.01}$	$3.60^{+0.03}_{-0.04}$	$0.27^{+0.06}_{-0.08}$	$2.07^{+0.29}_{-0.25}$	$1.24^{+0.01}_{-0.01}$	$208.35^{+14.37}_{-13.65}$	690/634
HB3	$1.98^{+0.06}_{-0.13}$	$1.94^{+0.03}_{-0.02}$	$3.47^{+0.05}_{-0.04}$	0.15 (fix)	$2.20^{+0.17}_{-0.17}$	$1.19^{+0.02}_{-0.02}$	$290.76^{+26.30}_{-21.14}$	710/635
HB4	$2.26^{+0.05}_{-0.05}$	$1.97^{+0.02}_{-0.02}$	$3.34^{+0.04}_{-0.04}$	0.21 (fix)	$2.91^{+0.24}_{-0.23}$	$1.17^{+0.01}_{-0.01}$	$506.54^{+41.56}_{-37.85}$	713/635
NB1	$2.28^{+0.03}_{-0.03}$	$2.04^{+0.02}_{-0.02}$	$3.25^{+0.03}_{-0.04}$	0.20 (fix)	$3.23^{+0.15}_{-0.18}$	$1.16^{+0.01}_{-0.01}$	$532.16^{+31.16}_{-34.35}$	840/635
NB2	$2.20^{+0.05}_{-0.04}$	$2.10^{+0.03}_{-0.04}$	$3.16^{+0.05}_{-0.05}$	0.19 (fix)	$2.94^{+0.39}_{-0.37}$	$1.09^{+0.04}_{-0.04}$	$717.26^{+55.84}_{-51.47}$	771/635
NB3	$2.21^{+0.04}_{-0.04}$	$2.20^{+0.06}_{-0.07}$	$3.08^{+0.03}_{-0.05}$	0.20 (fix)	$3.16^{+0.22}_{-0.22}$	$1.08^{+0.01}_{-0.01}$	$691.48^{+41.88}_{-38.02}$	754/635
NB4	$2.26^{+0.04}_{-0.04}$	$2.36^{+0.03}_{-0.03}$	$2.99^{+0.04}_{-0.04}$	0.20 (fix)	$3.65^{+0.11}_{-0.23}$	$1.04^{+0.01}_{-0.01}$	$766.22^{+43.54}_{-41.99}$	761/635
FB1	$2.38^{+0.07}_{-0.06}$	$2.42^{+0.05}_{-0.05}$	$2.86^{+0.08}_{-0.08}$	0.21 (fix)	$3.33^{+0.38}_{-0.39}$	$1.05^{+0.01}_{-0.01}$	$775.05^{+48.17}_{-45.39}$	684/635
FB2	$2.21^{+0.07}_{-0.07}$	$2.45^{+0.06}_{-0.06}$	$2.86^{+0.19}_{-0.16}$	0.21 (fix)	$2.85^{+0.33}_{-0.26}$	$1.17^{+0.01}_{-0.01}$	$385.48^{+19.69}_{-18.18}$	830/635

## References

- Agrawal, V. K., and Anuj Nandi. 2020. AstroSat view of LMC X-2: evolution of broad-band X-ray spectral properties along a complete Z-track. *MNRAS* 497, no. 3 (September): 3726–3733. <https://doi.org/10.1093/mnras/staa2063>. arXiv: 2007.05938 [astro-ph.HE].
- Agrawal, V. K., Anuj Nandi, V. Girish, and M. C. Ramadevi. 2018. Spectral and timing properties of atoll source 4U 1705-44: LAXPC/AstroSat results. *MNRAS* 477, no. 4 (July): 5437–5446. <https://doi.org/10.1093/mnras/sty1005>. arXiv: 1804.08371 [astro-ph.HE].
- Agrawal, V. K., Anuj Nandi, and M. C. Ramadevi. 2020. AstroSat/LAXPC view of GX 17+2: spectral evolution along the Z-track. *Ap&SS* 365, no. 2 (February): 41. <https://doi.org/10.1007/s10509-020-3748-0>. arXiv: 2002.04489 [astro-ph.HE].
- Agrawal, V. K., and P. Sree Kumar. 2003. X-ray spectral evolution of low-mass X-ray binary GX 349+2. *MNRAS* 346, no. 3 (December): 933–939. <https://doi.org/10.1111/j.1365-2966.2003.07147.x>. arXiv: astro-ph/0302581 [astro-ph].
- Agrawal, Vivek K., Anuj Nandi, and Tilak Katoch. 2023. AstroSat view of ‘Clocked’ burster GS 1826-238: broad-band spectral nature of persistent and burst emission during soft state. *MNRAS* 518, no. 1 (January): 194–205. <https://doi.org/10.1093/mnras/stac2579>. arXiv: 2209.08275 [astro-ph.HE].
- Altamirano, D., A. Ingram, M. van der Klis, R. Wijnands, M. Linares, and J. Homan. 2012. Low-frequency Quasi-periodic Oscillation from the 11 Hz Accreting Pulsar in Terzan 5: Not Frame Dragging. *ApJL* 759, no. 1 (November): L20. <https://doi.org/10.1088/2041-8205/759/1/L20>. arXiv: 1210.1494 [astro-ph.HE].
- Bańcuńska-Church, M., N. S. Schulz, J. Wilms, A. Gibiec, M. Hanke, R. E. Spencer, A. Rushton, and M. J. Church. 2011. Dipping in Cygnus X-2 in a multi-wavelength campaign due to absorption of extended ADC emission. *A&A* 530 (June): A102. <https://doi.org/10.1051/0004-6361/201015931>. arXiv: 1104.1715 [astro-ph.HE].
- Barret, D., J. F. Olive, L. Boirin, C. Done, G. K. Skinner, and J. E. Grindlay. 2000. Hard X-Ray Emission from Low-Mass X-Ray Binaries. *ApJ* 533, no. 1 (April): 329–351. <https://doi.org/10.1086/308651>. arXiv: astro-ph/9911042 [astro-ph].
- Barret, Didier. 2001. The broad band x-ray/hard x-ray spectra of accreting neutron stars. *Advances in Space Research* 28, nos. 2-3 (January): 307–321. [https://doi.org/10.1016/S0273-1177\(01\)00414-8](https://doi.org/10.1016/S0273-1177(01)00414-8). arXiv: astro-ph/0101295 [astro-ph].
- . 2012. kHz Quasi-periodic Oscillations from the 2000 and 2010 X-Ray Transients Located in the Globular Cluster Terzan 5: EXO1745-248 and IGR J17480-2446. *ApJ* 753, no. 1 (July): 84. <https://doi.org/10.1088/0004-637X/753/1/84>. arXiv: 1205.0564 [astro-ph.HE].

**Table 3.** Best fit parameters obtained by fitting the spectra of different sections of the Z-track using model *tbabs(nthComp+diskbb)* (**Model 3**). The parameters of the fits are  $N_H$  in units of  $10^{22} \text{ cm}^{-2}$ , photon index  $\Gamma$ , electron temperature  $kT_e$ , disk temperature  $kT_{in}$ , normalization of Comptonized component  $N_{comp}$ , seed photon temperature  $kT_s$ , disk normalization  $N_{MCD}$ .

HID-Sections		Parameters						
–	$N_H$	$\Gamma$	$kT_e$ (keV)	$kT_s$ (keV)	$N_{COMP}$	$kT_{in}$ (keV)	$N_{MCD} (\times 10^4)$	$\chi^2/dof$
HB1	$1.94^{+0.07}_{-0.07}$	$2.73^{+0.03}_{-0.04}$	$4.82^{+0.11}_{-0.15}$	$0.87^{+0.01}_{-0.02}$	$0.51^{+0.03}_{-0.03}$	$0.41^{+0.02}_{-0.02}$	$0.90^{+0.44}_{-0.29}$	660/632
HB2	$2.05^{+0.07}_{-0.06}$	$2.77^{+0.03}_{-0.01}$	$4.59^{+0.13}_{-0.13}$	$0.89^{+0.02}_{-0.02}$	$0.54^{+0.02}_{-0.03}$	$0.41^{+0.02}_{-0.02}$	$1.11^{+0.53}_{-0.35}$	663/632
HB3	$2.25^{+0.08}_{-0.07}$	$2.78^{+0.03}_{-0.02}$	$4.45^{+0.16}_{-0.14}$	$0.88^{+0.02}_{-0.02}$	$0.66^{+0.04}_{-0.04}$	$0.36^{+0.02}_{-0.02}$	$2.74^{+1.70}_{-1.14}$	686/632
HB4	$2.83^{+0.11}_{-0.11}$	$2.99^{+0.04}_{-0.05}$	$4.43^{+0.18}_{-0.16}$	$0.86^{+0.02}_{-0.02}$	$1.06^{+0.05}_{-0.05}$	$0.32^{+0.01}_{-0.01}$	$12.53^{+4.44}_{-3.21}$	666/632
NB1	$2.90^{+0.06}_{-0.07}$	$3.13^{+0.05}_{-0.06}$	$4.29^{+0.14}_{-0.16}$	$0.87^{+0.01}_{-0.01}$	$1.09^{+0.04}_{-0.05}$	$0.30^{+0.01}_{-0.01}$	$20.10^{+4.95}_{-4.25}$	712/632
NB2	$2.92^{+0.07}_{-0.05}$	$3.45^{+0.06}_{-0.06}$	$4.76^{+0.28}_{-0.29}$	$0.82^{+0.01}_{-0.01}$	$1.26^{+0.07}_{-0.08}$	$0.29^{+0.01}_{-0.01}$	$27.74^{+5.55}_{-3.69}$	732/632
NB3	$2.74^{+0.07}_{-0.06}$	$3.50^{+0.06}_{-0.07}$	$4.22^{+0.17}_{-0.29}$	$0.85^{+0.02}_{-0.01}$	$1.03^{+0.06}_{-0.05}$	$0.32^{+0.01}_{-0.01}$	$12.23^{+4.85}_{-2.20}$	698/632
NB4	$2.79^{+0.06}_{-0.06}$	$3.84^{+0.08}_{-0.08}$	$4.31^{+0.27}_{-0.31}$	$0.84^{+0.01}_{-0.01}$	$1.08^{+0.06}_{-0.06}$	$0.30^{+0.01}_{-0.01}$	$16.92^{+3.59}_{-3.48}$	709/632
FB1	$2.78^{+0.11}_{-0.10}$	$3.75^{+0.20}_{-0.22}$	$3.41^{+0.44}_{-0.30}$	$0.85^{+0.02}_{-0.02}$	$1.01^{+0.07}_{-0.07}$	$0.31^{+0.02}_{-0.02}$	$11.53^{+6.98}_{-4.31}$	654/632
FB2	$2.63^{+0.15}_{-0.12}$	$4.14^{+0.28}_{-0.39}$	$3.58^{+0.58}_{-0.39}$	$0.94^{+0.02}_{-0.02}$	$0.63^{+0.04}_{-0.04}$	$0.34^{+0.03}_{-0.02}$	$6.13^{+3.18}_{-1.53}$	806/632

**Table 4.** Best fit parameters obtained by fitting the spectra of different sections of the Z-track using model *tbabs(Comptb+diskbb)* (**Model 4**). The parameters of the fits are  $N_H$  in units of  $10^{22} \text{ cm}^{-2}$ , energy index  $\alpha$ , electron temperature  $kT_e$ , disk temperature  $kT_{in}$ , normalization of Comptonized component  $N_{comp}$ , seed photon temperature  $kT_s$ , disk normalization  $N_{MCD}$ .

HID-Sections		Parameters						
–	$N_H$	$\alpha$	$kT_e$ (keV)	$kT_s$ (keV)	$N_{COMP}$	$kT_{in}$ (keV)	$N_{MCD} (\times 10^4)$	$\chi^2/dof$
HB1	$1.94^{+0.07}_{-0.07}$	$1.81^{+0.05}_{-0.04}$	$4.47^{+0.13}_{-0.12}$	$0.89^{+0.02}_{-0.02}$	$0.10^{+0.01}_{-0.01}$	$0.42^{+0.02}_{-0.03}$	$0.87^{+0.45}_{-0.34}$	661/632
HB2	$2.04^{+0.07}_{-0.07}$	$1.84^{+0.04}_{-0.05}$	$4.25^{+0.11}_{-0.10}$	$0.92^{+0.02}_{-0.02}$	$0.12^{+0.01}_{-0.01}$	$0.40^{+0.02}_{-0.02}$	$1.08^{+0.48}_{-0.34}$	664/632
HB3	$2.25^{+0.12}_{-0.11}$	$1.85^{+0.04}_{-0.05}$	$4.11^{+0.12}_{-0.13}$	$0.88^{+0.02}_{-0.02}$	$0.13^{+0.01}_{-0.02}$	$0.36^{+0.02}_{-0.03}$	$2.73^{+1.91}_{-1.18}$	685/632
HB4	$2.92^{+0.1}_{-0.1}$	$2.08^{+0.05}_{-0.05}$	$4.12^{+0.12}_{-0.12}$	$0.90^{+0.01}_{-0.01}$	$0.20^{+0.01}_{-0.01}$	$0.32^{+0.01}_{-0.01}$	$13.02^{+6.05}_{-4.22}$	676/632
NB1	$3.05^{+0.07}_{-0.07}$	$2.23^{+0.06}_{-0.06}$	$3.97^{+0.13}_{-0.14}$	$0.90^{+0.01}_{-0.01}$	$0.21^{+0.02}_{-0.01}$	$0.30^{+0.01}_{-0.01}$	$21.62^{+6.10}_{-4.81}$	717/632
NB2	$2.98^{+0.15}_{-0.15}$	$2.54^{+0.08}_{-0.08}$	$4.35^{+0.26}_{-0.22}$	$0.86^{+0.02}_{-0.01}$	$0.19^{+0.01}_{-0.01}$	$0.28^{+0.01}_{-0.01}$	$27.48^{+5.64}_{-3.59}$	735/632
NB3	$2.79^{+0.08}_{-0.08}$	$2.55^{+0.09}_{-0.09}$	$3.74^{+0.17}_{-0.16}$	$0.88^{+0.01}_{-0.01}$	$0.17^{+0.01}_{-0.01}$	$0.32^{+0.01}_{-0.01}$	$12.09^{+4.21}_{-3.22}$	704/632
NB4	$2.75^{+0.07}_{-0.07}$	$2.79^{+0.10}_{-0.11}$	$3.56^{+0.21}_{-0.18}$	$0.86^{+0.01}_{-0.01}$	$0.16^{+0.01}_{-0.01}$	$0.33^{+0.01}_{-0.01}$	$9.56^{+3.44}_{-2.57}$	712/632
FB1	$2.87^{+0.11}_{-0.12}$	$3.11^{+0.23}_{-0.25}$	$3.36^{+0.41}_{-0.29}$	$0.89^{+0.02}_{-0.02}$	$0.16^{+0.01}_{-0.01}$	$0.32^{+0.02}_{-0.02}$	$13.94^{+7.22}_{-4.81}$	658/632
FB2	$2.69^{+0.12}_{-0.11}$	$3.32^{+0.32}_{-0.36}$	$3.35^{+0.57}_{-0.44}$	$0.97^{+0.02}_{-0.01}$	$0.13^{+0.01}_{-0.01}$	$0.34^{+0.03}_{-0.02}$	$7.03^{+3.94}_{-2.57}$	808/632

**Table 5.** The table provides the Comptonization flux  $F_{Comp}$  and disk flux  $F_{dbb}$  in the energy range 0.5 – 50.0 keV. All the fluxes are in units of  $10^{-9}$  ergs/s/cm<sup>2</sup>. The disk radius  $R_{eff}$ , seed photon radius  $R_s$ , optical depth  $\tau$  and color correction factor are also given. See text for details. The derived values are for the **Model 4**

HID-Sections	Derived fluxes and parameters							
	$F_{Comp}$	$F_{dbb}$	$R_{eff}(km)$	$R_{in}(km)$	$R_s(km)$	$\tau$	y-par	f
HB1	10.72±0.25	3.80±0.28	252.86 <sup>+69.54</sup> <sub>-47.58</sub>	82.22 <sup>+21.40</sup> <sub>-14.58</sub>	24.46 <sup>+1.28</sup> <sub>-1.28</sub>	4.95 <sup>+0.25</sup> <sub>-0.21</sub>	0.85±0.08	1.75
HB2	11.76±0.27	4.27±0.49	286.55 <sup>+66.29</sup> <sub>-46.81</sub>	91.81 <sup>+20.46</sup> <sub>-14.45</sub>	24.06 <sup>+1.18</sup> <sub>-1.18</sub>	5.03 <sup>+0.20</sup> <sub>-0.22</sub>	0.84±0.07	1.77
HB3	13.49±0.31	5.75±1.09	468.13 <sup>+168.57</sup> <sub>-102.74</sub>	145.63 <sup>+52.03</sup> <sub>-31.71</sub>	28.13 <sup>+1.47</sup> <sub>-1.47</sub>	5.14 <sup>+0.25</sup> <sub>-0.26</sub>	0.84±0.08	1.79
HB4	18.20±0.35	15.14±1.09	1112.75 <sup>+238.95</sup> <sub>-173.55</sub>	317.63 <sup>+73.75</sup> <sub>+51.50</sub>	32.70 <sup>+1.64</sup> <sub>-1.64</sub>	4.61 <sup>+0.21</sup> <sub>-0.21</sub>	0.68±0.06	1.87
NB1	18.62±0.41	20.42±0.88	1468.04 <sup>+219.56</sup> <sub>-173.55</sub>	409.10 <sup>+67.71</sup> <sub>-53.54</sub>	33.83 <sup>+1.10</sup> <sub>-1.11</sub>	4.44 <sup>+0.23</sup> <sub>-0.24</sub>	0.61±0.06	1.89
NB2	16.60±0.39	18.20±1.19	1626.58 <sup>+177.68</sup> <sub>-113.10</sub>	461.28 <sup>+54.34</sup> <sub>-34.91</sub>	36.62 <sup>+2.06</sup> <sub>-2.05</sub>	3.72 <sup>+0.32</sup> <sub>-0.28</sub>	0.47±0.08	1.88
NB3	14.79±0.33	14.13±0.63	1049.09 <sup>+175.96</sup> <sub>-131.70</sub>	306.09 <sup>+54.31</sup> <sub>-40.65</sub>	32.84 <sup>+1.22</sup> <sub>-1.22</sub>	4.08 <sup>+0.32</sup> <sub>-0.30</sub>	0.48±0.07	1.85
NB4	13.49±0.30	12.30±0.42	916.23 <sup>+158.92</sup> <sub>-118.61</sub>	272.13 <sup>+49.03</sup> <sub>-36.61</sub>	33.64 <sup>+1.31</sup> <sub>-1.30</sub>	3.87 <sup>+0.37</sup> <sub>-0.37</sub>	0.41±0.06	1.83
FB1	12.59±0.28	13.80±0.54	1110.26 <sup>+276.82</sup> <sub>-185.03</sub>	328.57 <sup>+85.54</sup> <sub>-57.11</sub>	31.16 <sup>+2.13</sup> <sub>-2.11</sub>	3.61 <sup>+0.67</sup> <sub>-0.60</sub>	0.34±0.12	1.84
FB2	10.25±0.21	8.91±0.63	749.26 <sup>+212.02</sup> <sub>-138.31</sub>	233.34 <sup>+65.44</sup> <sub>-42.69</sub>	24.02 <sup>+2.26</sup> <sub>-2.46</sub>	3.40 <sup>+1.10</sup> <sub>-0.79</sub>	0.30±0.16	1.79

**Table 6.** Fit-Statistics to compare 3 different models used to describe the X-ray spectra of the source. We have compared Model-3 with Model-1 and Model-2 by computing F-test chance improvement probabilities

Segment	$\chi^2/dof( Model - 4)$	$\chi^2/dof( Model-1)$	$\chi^2/dof( Model-2)$	F-test Prob (Model-4 vs Model-1)	F-test (Model-4 vs Model-2)
HB1	661/632	686/633	696/634	$1.3 \times 10^{-6}$	$8.30 \times 10^{-8}$
HB2	664/632	697/633	690/634	$3.1 \times 10^{-8}$	$5.3 \times 10^{-7}$
HB3	685/632	720/633	710/635	$2.0 \times 10^{-8}$	$4.7 \times 10^{-5}$
HB4	676/632	754/634	713/635	$1.1 \times 10^{-16}$	$2.2 \times 10^{-7}$
NB1	717/632	930/634	840/635	$2.0 \times 10^{-36}$	$1.4 \times 10^{-21}$
NB2	735/632	810/634	771/635	$4.6 \times 10^{-14}$	$1.2 \times 10^{-6}$
NB3	704/632	821/634	754/635	$7.9 \times 10^{-22}$	$2.0 \times 10^{-9}$
NB4	712/632	814/634	761/635	$4.2 \times 10^{-19}$	$3.8 \times 10^{-9}$
FB1	658/632	725/634	684/635	$4.9 \times 10^{-14}$	$1.9 \times 10^{-5}$
FB2	808/632	837/634	830/635	$1.4 \times 10^{-5}$	$7.0 \times 10^{-4}$

Belloni, Tomaso, Dimitrios Psaltis, and Michiel van der Klis. 2002. A Unified Description of the Timing Features of Accreting X-Ray Binaries. *ApJ* 572, no. 1 (June): 392–406. <https://doi.org/10.1086/340290>. arXiv: astro-ph/0202213 [astro-ph].

Bhargava, Yash, Sudip Bhattacharyya, Jeroen Homan, and Mayukh Pahari. 2023. AstroSat View of the Neutron Star Low-mass X-Ray Binary GX 340+0. *ApJ* 955, no. 2 (October): 102. <https://doi.org/10.3847/1538-4357/acee7a>. arXiv: 2307.13979 [astro-ph.HE].

Bu, Qing-cui, Li Chen, Zhao-sheng Li, Jin-lu Qu, T. M. Belloni, and Liang Zhang. 2015. Correlations in Horizontal Branch Oscillations and Break Components in XTE J1701–462 and GX 17+2. *ApJ* 799, no. 1 (January): 2. <https://doi.org/10.1088/0004-637X/799/1/2>. arXiv: 1411.1137 [astro-ph.HE].

Cabanac, C., G. Henri, P. -O. Petrucci, J. Malzac, J. Ferreira, and T. M. Belloni. 2010. Variability of X-ray binaries from an oscillating hot corona. *MNRAS* 404, no. 2 (May): 738–748. <https://doi.org/10.1111/j.1365-2966.2010.16340.x>. arXiv: 1001.2116 [astro-ph.HE].

Chakrabarti, Sandip, and Lev G. Titarchuk. 1995. Spectral Properties of Accretion Disks around Galactic and Extragalactic Black Holes. *ApJ* 455 (December): 623. <https://doi.org/10.1086/176610>. arXiv: astro-ph/9510005 [astro-ph].

Chakrabarti, Sandip K. 1997. Spectral Properties of Accretion Disks around Black Holes. II. Sub-Keplerian Flows with and without Shocks. *ApJ* 484, no. 1 (July): 313–322. <https://doi.org/10.1086/304325>. arXiv: astro-ph/9706001 [astro-ph].

Chakraborty, Manoneeta, Sudip Bhattacharyya, and Arunava Mukherjee. 2011. Terzan 5 transient IGR J17480–2446: variation of burst and spectral properties with spectral states. *MNRAS* 418, no. 1 (November): 490–499. <https://doi.org/10.1111/j.1365-2966.2011.19499.x>. arXiv: 1102.1033 [astro-ph.HE].

Cocchi, Massimo, Andrea Gnarini, Sergio Fabiani, Francesco Ursini, Juri Poutanen, Fiamma Capitanio, Anna Bobrikova, et al. 2023. Discovery of strongly variable X-ray polarization in the neutron star low-mass X-ray binary transient XTE J1701–462. *A&A* 674 (June): L10. <https://doi.org/10.1051/0004-6361/202346275>. arXiv: 2306.10965 [astro-ph.HE].

Coughenour, Benjamin M., Edward M. Cackett, Jon M. Miller, and Renee M. Ludlam. 2018. A NuSTAR Observation of the Low-mass X-Ray Binary GX 349+2 throughout the Z-track. *ApJ* 867, no. 1 (November): 64. <https://doi.org/10.3847/1538-4357/aae098>. arXiv: 1708.01652 [astro-ph.HE].

Davis, Shane W., and Samer El-Abd. 2019. Spectral Hardening in Black Hole Accretion: Giving Spectral Modelers an f. *ApJ* 874, no. 1 (March): 23. <https://doi.org/10.3847/1538-4357/ab05c5>. arXiv: 1809.05134 [astro-ph.HE].

Di Salvo, T., R. Farinelli, L. Burderi, F. Frontera, E. Kuulkers, N. Masetti, N. R. Robba, L. Stella, and M. van der Klis. 2002. On the spectral evolution of Cygnus X-2 along its color-color diagram. *A&A* 386 (May): 535–547. <https://doi.org/10.1051/0004-6361:20020238>. arXiv: astro-ph/0202295 [astro-ph].

**Table 7.** Parameter values obtained by fitting the PDS of different segments of the Z-track. Lorentzian components and power-law are required to describe the BLN, narrow QPOs and VLFN in the PDS. The parameters of the fit are, power-law index  $\alpha$ , break frequency  $\nu_{break}$ , the characteristics frequency of the QPOs  $\nu_{char}$  ( $\nu_{HBO}$  for HBO and  $\nu_{NBO}$  for NBO) and full-width half-maxima  $\Delta\nu$ .

Segment	$\alpha$	$\nu_{break}$	$\nu_{NBO}$ (significance)	$\Delta\nu_{NBO}$	$\nu_{HBO}$ (significance)	$\Delta\nu_{HBO}$	$\chi^2/dof$
HB1	$0.74^{+0.02}_{-0.02}$	$6.46^{+0.26}_{-0.24}$	–	–	$34.31^{+0.25}_{-0.25}$ (12.7 $\sigma$ )	$7.42^{+0.85}_{-0.76}$	122/163
HB2	$0.85^{+0.03}_{-0.02}$	$7.01^{+0.21}_{-0.20}$	–	–	$39.06^{+0.47}_{-0.45}$ (10.8 $\sigma$ )	$12.33^{+1.59}_{-1.39}$	159/163
HB3	$0.82^{+0.02}_{-0.02}$	$7.24^{+0.31}_{-0.32}$	–	–	$41.49^{+0.71}_{-0.68}$ (5.8 $\sigma$ )	$8.45^{+2.10}_{-1.76}$	118/163
HB4	$0.93^{+0.07}_{-0.06}$	$10.98^{+1.01}_{-0.90}$	–	–	$59.51^{+3.86}_{-3.95}$ (2.6 $\sigma$ )	$19.95^{+10.97}_{-9.23}$	97/163
NB1	$1.14^{+0.09}_{-0.08}$	–	$9.62^{+1.20a}_{-0.85}$	$11.18^{+4.15b}_{-2.94}$	$58.20^{+5.70c}_{-4.92}$	$41.11^{+22.52d}_{-14.14}$	143/162
NB2	$1.21^{+0.17}_{-0.17}$	–	$6.67^{+0.16}_{-0.10}$ (3.0 $\sigma$ )	$2.74^{+1.65}_{-1.04}$	–	–	121/165
NB3	$1.67^{+0.11}_{-0.10}$	–	$6.68^{+0.06}_{-0.04}$ (5.8 $\sigma$ )	$2.45^{+0.71}_{-0.45}$	–	–	115/165
NB4	$1.36^{+0.10}_{-0.09}$	–	–	–	–	–	143/168
FB1	$1.27^{+0.15}_{-0.13}$	–	–	–	–	–	110/168
FB2	$1.69^{+0.15}_{-0.13}$	–	–	–	–	–	118/168

a. The frequency of LFN

b. FWHM of LFN

c. Frequency of HFN

d. FWHM of HFN

**Table 8.** The table provides the rms strength (in %) of different power spectral features (VLFN, BLN and narrow QPOs) as a function of HID position.

Segments	VLFN-rms	Break-rms	HBO-rms	NBO-rms
HB1	$6.86^{+0.32}_{-0.33}$	$8.49^{+0.14}_{-0.13}$	$4.49^{+0.16}_{-0.18}$	–
HB2	$5.6^{+0.27}_{-0.23}$	$8.19^{+0.12}_{-0.13}$	$4.04^{+0.19}_{-0.17}$	–
HB3	$6.57^{+0.33}_{-0.28}$	$7.68^{+0.15}_{-0.15}$	$2.77^{+0.23}_{-0.23}$	–
HB4	$4.25^{+0.38}_{-0.37}$	$5.23^{+0.25}_{-0.24}$	$2.25^{+0.42}_{-0.36}$	–
NB1	$2.71^{+0.37}_{-0.35}$	–	$2.82^{+0.37a}_{-0.32}$	$2.32^{+0.32b}_{-0.25}$
NB2	$2.30^{+0.27}_{-0.27}$	–	–	$1.64^{+0.26}_{-0.25}$
NB3	$1.84^{+0.17}_{-0.16}$	–	–	$1.66^{+0.15}_{-0.14}$
NB4	$1.76^{+0.12}_{-0.13}$	–	–	–
FB1	$2.41^{+0.22}_{-0.23}$	–	–	–
FB2	$3.35^{+0.40}_{-0.37}$	–	–	–

a. HFN-rms

b. LFN-rms

- Di Salvo, T., N. R. Robba, R. Iaria, L. Stella, L. Burderi, and G. L. Israel. 2001. Detection of a Hard Tail in the X-Ray Spectrum of the Z Source GX 349+2. *Aj* 554, no. 1 (June): 49–55. <https://doi.org/10.1086/321353>. arXiv: astro-ph/0102299 [astro-ph].
- Ding, G. Q., S. N. Zhang, N. Wang, J. L. Qu, and S. P. Yan. 2011. On the Nature of the First Transient Z Source XTE J1701–462: Its Accretion Disk Structure, Neutron Star Magnetic Field Strength, and Hard Tail. *Aj* 142, no. 2 (August): 34. <https://doi.org/10.1088/0004-6256/142/2/34>. arXiv: 1105.5617 [astro-ph.HE].
- Farinelli, Ruben, Lev Titarchuk, Ada Paizis, and Filippo Frontera. 2008. A New Comptonization Model for Weakly Magnetized, Accreting Neutron Stars in Low-Mass X-Ray Binaries. *Aj* 680, no. 1 (June): 602–614. <https://doi.org/10.1086/587162>. arXiv: 0802.2639 [astro-ph].
- Fridriksson, Joel K., Jeroen Homan, and Ronald A. Remillard. 2015. Common Patterns in the Evolution between the Luminous Neutron Star Low-Mass X-ray Binary Subclasses. *Aj* 809, no. 1 (August): 52. <https://doi.org/10.1088/0004-637X/809/1/52>. arXiv: 1504.00022 [astro-ph.HE].
- Gierliński, Marek, and Chris Done. 2002. The X-ray spectrum of the atoll source 4U 1608–52. *MNRAS* 337, no. 4 (December): 1373–1380. <https://doi.org/10.1046/j.1365-8711.2002.06009.x>. arXiv: astro-ph/0208389 [astro-ph].
- Hasinger, G. 1987. A classification of fast quasi-periodic X-ray oscillators: is 6 Hz a fundamental frequency? *A&A* 186 (November): 153–158.
- Hasinger, G., and M. van der Klis. 1989. Two patterns of correlated X-ray timing and spectral behaviour in low-mass X-ray binaries. *A&A* 225 (November): 79–96.
- Hasinger, G., M. van der Klis, K. Ebisawa, T. Dotani, and K. Mitsuda. 1990. Multifrequency observations of Cygnus X-2: X-ray observations with Ginga. *A&A* 235 (August): 131.
- Homan, Jeroen, Michiel van der Klis, Joel K. Fridriksson, Ronald A. Remillard, Rudy Wijnands, Mariano Méndez, Dacheng Lin, et al. 2010. XTE J1701–462 and Its Implications for the Nature of Subclasses in Low-magnetic-field Neutron Star Low-mass X-ray Binaries. *Aj* 719, no. 1 (August): 201–212. <https://doi.org/10.1088/0004-637X/719/1/201>. arXiv: 1005.3210 [astro-ph.HE].
- Homan, Jeroen, Michiel van der Klis, Peter G. Jonker, Rudy Wijnands, Erik Kuulkers, Mariano Méndez, and Walter H. G. Lewin. 2002. RXTE Observations of the Neutron Star Low-Mass X-Ray Binary GX 17+2: Correlated X-Ray Spectral and Timing Behavior. *Aj* 568, no. 2 (April): 878–900. <https://doi.org/10.1086/339057>. arXiv: astro-ph/0104323 [astro-ph].

**Table 9.** Energy dependent rms values (in %) of BLN and HBO components in the PDS.

Energy-band	HBO-rms			Break-rms		
	HB1	HB2	HB3	HB1	HB2	HB3
3 – 5 keV	2.66 <sup>+0.48</sup> <sub>-0.39</sub>	2.72 <sup>+0.66</sup> <sub>-0.42</sub>	< 1.97	6.79 <sup>+0.33</sup> <sub>-0.46</sub>	5.96 <sup>+0.26</sup> <sub>-0.30</sub>	5.54 <sup>+0.45</sup> <sub>-0.54</sub>
5 – 8 keV	5.59 <sup>+0.54</sup> <sub>-0.49</sub>	3.28 <sup>+0.67</sup> <sub>-0.54</sub>	2.68 <sup>+0.55</sup> <sub>-0.37</sub>	10.09 <sup>+0.42</sup> <sub>-0.42</sub>	9.38 <sup>+0.36</sup> <sub>-0.34</sub>	8.75 <sup>+0.40</sup> <sub>-0.40</sub>
8 – 15 keV	7.73 <sup>+0.64</sup> <sub>-0.60</sub>	7.04 <sup>+0.80</sup> <sub>-0.78</sub>	4.94 <sup>+1.31</sup> <sub>-0.92</sub>	14.66 <sup>+0.37</sup> <sub>-0.37</sub>	13.71 <sup>+0.43</sup> <sub>-0.43</sub>	12.20 <sup>+0.53</sup> <sub>-0.49</sub>

- Homan, Jeroen, Michiel van der Klis, Rudy Wijnands, Tomaso Belloni, Rob Fender, Marc Klein-Wolt, Piergiorgio Casella, et al. 2007. Rossi X-Ray Timing Explorer Observations of the First Transient Z Source XTE J1701-462: Shedding New Light on Mass Accretion in Luminous Neutron Star X-Ray Binaries. *ApJ* 656, no. 1 (February): 420–430. <https://doi.org/10.1086/510447>. arXiv: astro-ph/0611083 [astro-ph].
- Huang, Y., J. L. Qu, S. N. Zhang, Q. C. Bu, Y. P. Chen, L. Tao, S. Zhang, et al. 2018. INSIGHT-HXMT Observations of the New Black Hole Candidate MAXI J1535-571: Timing Analysis. *ApJ* 866, no. 2 (October): 122. <https://doi.org/10.3847/1538-4357/aade4c>. arXiv: 1808.05318 [astro-ph.HE].
- Iaria, R., T. di Salvo, N. R. Robba, L. Burderi, G. Lavagetto, L. Stella, F. Frontera, and M. van der Klis. 2004. A new BeppoSAX observation of the Z Source GX 349+2. *Nuclear Physics B Proceedings Supplements* 132 (June): 608–611. <https://doi.org/10.1016/j.nuclphysbps.2004.04.104>.
- in 't Zand, J. J. M., F. Verbunt, T. E. Strohmayer, A. Bazzano, M. Cocchi, J. Heise, M. H. van Kerkwijk, et al. 1999. A new X-ray outburst in the globular cluster NGC 6440: SAX J1748.9-2021. *A&A* 345 (May): 100–108. <https://doi.org/10.48550/arXiv.astro-ph/9902319>. arXiv: astro-ph/9902319 [astro-ph].
- Ingram, Adam, Chris Done, and P. Chris Fragile. 2009. Low-frequency quasi-periodic oscillations spectra and Lense-Thirring precession. *MNRAS* 397, no. 1 (July): L101–L105. <https://doi.org/10.1111/j.1745-3933.2009.00693.x>. arXiv: 0901.1238 [astro-ph.SR].
- Iwakiri, W., M. Serino, H. Negoro, M. Nakajima, K. Kobayashi, M. Tanaka, Y. Soejima, et al. 2022. MAXI/GSC detection of a new X-ray outburst from XTE J1701-462. *The Astronomer's Telegram* 15592 (September): 1.
- Jayasurya, Kiran M., Vivek K. Agrawal, and Rwitika Chatterjee. 2023. Detection of significant X-ray polarization from transient NS-LMXB XTE J1701-462 with IXPE and its implication on the coronal geometry. *MNRAS* 525, no. 3 (November): 4657–4662. <https://doi.org/10.1093/mnras/stad2601>. arXiv: 2302.03396 [astro-ph.HE].
- Jonker, P. G., M. van der Klis, J. Homan, M. Méndez, W. H. G. Lewin, R. Wijnands, and W. Zhang. 2002. Low- and high-frequency variability as a function of spectral properties in the bright X-ray binary GX 5-1. *MNRAS* 333, no. 3 (July): 665–678. <https://doi.org/10.1046/j.1365-8711.2002.05442.x>. arXiv: astro-ph/0202420 [astro-ph].
- Jonker, Peter G., Michiel van der Klis, Rudy Wijnands, Jeroen Homan, Jan van Paradijs, Mariano Méndez, Eric C. Ford, Erik Kuulkers, and Frederick K. Lamb. 2000. The Power Spectral Properties of the Z Source GX 340+0. *ApJ* 537, no. 1 (July): 374–386. <https://doi.org/10.1086/309029>. arXiv: astro-ph/0002022 [astro-ph].
- Jonker, Peter G., Rudy Wijnands, Michiel van der Klis, Dimitrios Psaltis, Erik Kuulkers, and Frederick K. Lamb. 1998. Discovery of Kilohertz Quasi-periodic Oscillations in the Z Source GX 340+0. *ApJ Letters* 499, no. 2 (June): L191–L194. <https://doi.org/10.1086/311372>. arXiv: astro-ph/9804070 [astro-ph].
- Li, Zhaosheng, Li Chen, Jinlu Qu, Qingcui Bu, Dehua Wang, and Renxin Xu. 2014. The Accretion Rate Independence of Horizontal Branch Oscillation in XTE J1701-462. *786*, no. 2 (May): 119. <https://doi.org/10.1088/0004-637X/786/2/119>. arXiv: 1403.4672 [astro-ph.HE].
- Lin, Dacheng, Diego Altamirano, Jeroen Homan, Ronald A. Remillard, Rudy Wijnands, and Tomaso Belloni. 2009. Type I X-ray Bursts from the Neutron-star Transient XTE J1701-462. *ApJ* 699, no. 1 (July): 60–65. <https://doi.org/10.1088/0004-637X/699/1/60>. arXiv: 0904.2187 [astro-ph.HE].
- Lin, Dacheng, Ronald A. Remillard, and Jeroen Homan. 2007. Evaluating Spectral Models and the X-Ray States of Neutron Star X-Ray Transients. *ApJ* 667, no. 2 (October): 1073–1086. <https://doi.org/10.1086/521181>. arXiv: astro-ph/0702089 [astro-ph].
- . 2009. Spectral States of XTE J1701 - 462: Link Between Z and Atoll Sources. *ApJ* 696, no. 2 (May): 1257–1277. <https://doi.org/10.1088/0004-637X/696/2/1257>. arXiv: 0901.0031 [astro-ph.HE].
- Ludlam, R. M., E. M. Cackett, J. A. García, J. M. Miller, A. L. Stevens, A. C. Fabian, J. Homan, et al. 2022. Radius Constraints from Reflection Modeling of Cygnus X-2 with NuSTAR and NICER. *ApJ* 927, no. 1 (March): 112. <https://doi.org/10.3847/1538-4357/ac5028>. arXiv: 2201.11767 [astro-ph.HE].
- Majumder, Seshadri, H. Sreehari, Nafisa Aftab, Tilak Katoch, Santabrata Das, and Anuj Nandi. 2022. Wide-band view of high-frequency quasi-periodic oscillations of GRS 1915+105 in 'softer' variability classes observed with AstroSat. *MNRAS* 512, no. 2 (May): 2508–2524. <https://doi.org/10.1093/mnras/stac615>. arXiv: 2203.02710 [astro-ph.HE].
- Malu, S., K. Sriram, S. Harikrishna, and Vivek K. Agrawal. 2021. Exploring the inner-disc region of the atoll source 4U 1705-44 using AstroSat's SXT and LAXPC observations. *MNRAS* 506, no. 4 (October): 6203–6211. <https://doi.org/10.1093/mnras/stab1892>.
- Miller, M. Coleman, Frederick K. Lamb, and Dimitrios Psaltis. 1998. Sonic-Point Model of Kilohertz Quasi-periodic Brightness Oscillations in Low-Mass X-Ray Binaries. *ApJ* 508, no. 2 (December): 791–830. <https://doi.org/10.1086/306408>. arXiv: astro-ph/9609157 [astro-ph].
- Mitsuda, K., H. Inoue, K. Koyama, K. Makishima, M. Matsuoka, Y. Ogawara, N. Shibasaki, K. Suzuki, Y. Tanaka, and T. Hirano. 1984. Energy spectra of low-mass binary X-ray sources observed from Tenma. *PASJ* 36 (January): 741–759.
- Molteni, Diego, Hanno Sponholz, and Sandip K. Chakrabarti. 1996. Resonance Oscillation of Radiative Shock Waves in Accretion Disks around Compact Objects. *ApJ* 457 (February): 805. <https://doi.org/10.1086/176775>. arXiv: astro-ph/9508022 [astro-ph].
- Mondal, Aditya S., G. C. Dewangan, M. Pahari, and B. Raychaudhuri. 2018. NuSTAR view of the Z-type neutron star low-mass X-ray binary Cygnus X-2. *MNRAS* 474, no. 2 (February): 2064–2072. <https://doi.org/10.1093/mnras/stx2931>. arXiv: 1708.01032 [astro-ph.HE].
- Nandi, Anuj, Santabrata Das, Seshadri Majumder, Tilak Katoch, H. M. Antia, and Parag Shah. 2024. Discovery of evolving low-frequency QPOs in hard X-rays (100 keV) observed in black hole Swift J1727.8-1613 with AstroSat. *MNRAS* 531, no. 1 (June): 1149–1157. <https://doi.org/10.1093/mnras/stae1208>. arXiv: 2404.17160 [astro-ph.HE].
- Osherovich, Vladimir, and Lev Titarchuk. 1999. Kilohertz Quasi-periodic Oscillations in Neutron Star Binaries Modeled as Keplerian Oscillations in a Rotating Frame of Reference. *ApJ Letters* 522, no. 2 (September): L113–L116. <https://doi.org/10.1086/312225>. arXiv: astro-ph/9907360 [astro-ph].

- Remillard, R. A., D. Lin, ASM Team at MIT, and NASA/GSFC. 2006. New X-ray Transient, XTE J1701–462. *The Astronomer's Telegram* 696 (January): 1.
- Revnivtsev, M. G., and M. R. Gilfanov. 2006. Boundary layer emission and Z-track in the color-color diagram of luminous LMXBs. *A&A* 453, no. 1 (July): 253–259. <https://doi.org/10.1051/0004-6361:20053964>. arXiv: astro-ph/0506019 [astro-ph].
- Sanna, Andrea, Mariano Méndez, Diego Altamirano, Jeroen Homan, Piergiorgio Casella, Tomaso Belloni, Dacheng Lin, Michiel van der Klis, and Rudy Wijnands. 2010. The kilohertz quasi-periodic oscillations during the Z and atoll phases of the unique transient XTE J1701–462. *MNRAS* 408, no. 1 (October): 622–630. <https://doi.org/10.1111/j.1365-2966.2010.17145.x>. arXiv: 1005.3217 [astro-ph.HE].
- Schnerr, R. S., T. Reerink, M. van der Klis, J. Homan, M. Méndez, R. P. Fender, and E. Kuulkers. 2003. Peculiar spectral and power spectral behaviour of the LMXB GX 13+1. *A&A* 406 (July): 221–232. <https://doi.org/10.1051/0004-6361:20030682>. arXiv: astro-ph/0305161 [astro-ph].
- Shakura, N. I., and R. A. Sunyaev. 1973. Black holes in binary systems. Observational appearance. *A&A* 24 (January): 337–355.
- Shimura, Toshiya, and Fumio Takahara. 1995. On the Spectral Hardening Factor of the X-Ray Emission from Accretion Disks in Black Hole Candidates. *ApJ* 445 (June): 780. <https://doi.org/10.1086/175740>.
- Shirey, Robert E., Hale V. Bradt, and Alan M. Levine. 1999. The Complete “Z” Track of Circinus X-1. *ApJ* 517, no. 1 (May): 472–487. <https://doi.org/10.1086/307188>. arXiv: astro-ph/9901003 [astro-ph].
- Shyam Prakash, V. P., and Vivek K. Agrawal. 2024. AstroSat View of the Neutron Star Low-mass X-Ray Binary GX 5-1. *ApJ* 977, no. 2 (December): 215. <https://doi.org/10.3847/1538-4357/ad93b0>. arXiv: 2404.02782 [astro-ph.HE].
- Singh, Kulinder Pal, Gordon C. Stewart, Sunil Chandra, Kallol Mukerjee, Sanket Kotak, Andy P. Beardmore, Varsha Chitnis, et al. 2016. In-orbit performance of SXT aboard AstroSat. In *Space telescopes and instrumentation 2016: ultraviolet to gamma ray*, edited by Jan-Willem A. den Herder, Tadayuki Takahashi, and Marshall Bautz, vol. 9905, 99051E. Society of Photo-Optical Instrumentation Engineers (SPIE) Conference Series. July. <https://doi.org/10.1117/12.2235309>.
- Smale, Alan P., and Erik Kuulkers. 2000. LMC X-2: The First Extragalactic Z Source? *ApJ* 528, no. 2 (January): 702–710. <https://doi.org/10.1086/308193>. arXiv: astro-ph/9907303 [astro-ph].
- Sreehari, H., Anuj Nandi, Santabrata Das, V. K. Agrawal, Samir Mandal, M. C. Ramadevi, and Tilak Katoch. 2020. AstroSat view of GRS 1915+105 during the soft state: detection of HFQPOs and estimation of mass and spin. *MNRAS* 499, no. 4 (December): 5891–5901. <https://doi.org/10.1093/mnras/staa3135>. arXiv: 2010.03782 [astro-ph.HE].
- Stella, Luigi, and Mario Vietri. 1999. kHz Quasiperiodic Oscillations in Low-Mass X-Ray Binaries as Probes of General Relativity in the Strong-Field Regime. *PhRvL* 82, no. 1 (January): 17–20. <https://doi.org/10.1103/PhysRevLett.82.17>. arXiv: astro-ph/9812124 [astro-ph].
- Titarchuk, L. G., C. F. Bradshaw, B. J. Geldzahler, and E. B. Fomalont. 2001. Normal-Branch Quasi-periodic Oscillations in Scorpius X-1: Viscous Oscillations of a Spherical Shell Near the Neutron Star. *ApJ Letters* 555, no. 1 (July): L45–L48. <https://doi.org/10.1086/323160>. arXiv: astro-ph/0105559 [astro-ph].
- Titarchuk, Lev, Iosif Lapidus, and Alexander Muslimov. 1998. Mechanisms for High-Frequency Quasi-periodic Oscillations in Neutron Star and Black Hole Binaries. *ApJ* 499, no. 1 (May): 315–328. <https://doi.org/10.1086/305642>. arXiv: astro-ph/9712348 [astro-ph].
- van den Eijnden, Jakob, Adam Ingram, and Phil Uttley. 2016. Probing the origin of quasi-periodic oscillations: the short-time-scale evolution of phase lags in GRS 1915+105. *MNRAS* 458, no. 4 (June): 3655–3666. <http://doi.org/10.1093/mnras/stw610>. arXiv: 1603.03392 [astro-ph.HE].
- van der Klis, M. 2006. Rapid X-ray Variability. In *Compact stellar x-ray sources*, 39:39–112.
- Wijnands, Rudy, Mariano Méndez, Michiel van der Klis, Dimitrios Psaltis, Erik Kuulkers, and Frederick K. Lamb. 1998. Discovery of Kilohertz Quasi-periodic Oscillations in the Z Source GX 5-1. *ApJ Letters* 504, no. 1 (September): L35–L38. <https://doi.org/10.1086/311564>. arXiv: astro-ph/9806050 [astro-ph].
- Wilms, J., A. Allen, and R. McCray. 2000. On the Absorption of X-Rays in the Interstellar Medium. *ApJ* 542, no. 2 (October): 914–924. <https://doi.org/10.1086/317016>. arXiv: astro-ph/0008425 [astro-ph].
- Yadav, J. S., P. C. Agrawal, H. M. Antia, Jai Verdhhan Chauhan, Dhiraj Dedhia, Tilak Katoch, P. Madhwani, et al. 2016. Large Area X-ray Proportional Counter (LAXPC) instrument onboard ASTROSAT. In *Space telescopes and instrumentation 2016: ultraviolet to gamma ray*, edited by Jan-Willem A. den Herder, Tadayuki Takahashi, and Marshall Bautz, 9905:99051D. Society of Photo-Optical Instrumentation Engineers (SPIE) Conference Series. July. <https://doi.org/10.1117/12.2231857>.
- Yu, Wei, Qing-Cui Bu, Shuang-Nan Zhang, He-Xin Liu, Liang Zhang, Lorenzo Ducci, Lian Tao, et al. 2024. Timing analysis of the newly discovered black hole candidate Swift J1727.8–1613 with Insight-HXMT. *MNRAS* 529, no. 4 (April): 4624–4632. <https://doi.org/10.1093/mnras/stae835>. arXiv: 2403.13127 [astro-ph.HE].
- Yu, Wei, Qingcui Bu, Victor Doroshenko, Lorenzo Ducci, Long Ji, Wenda Zhang, Andrea Santangelo, et al. 2024. Correlated spectro-polarimetric study along the Z track in XTE J1701–462 puts constraints on its coronal geometry. *arXiv e-prints* (January): arXiv:2401.02658. <https://doi.org/10.48550/arXiv.2401.02658>. arXiv: 2401.02658 [astro-ph.HE].
- Zdziarski, A. A., W. N. Johnson, and P. Magdziarz. 1996. Broad-band  $\gamma$ -ray and X-ray spectra of NGC 4151 and their implications for physical processes and geometry. *MNRAS* 283, no. 1 (November): 193–206. <https://doi.org/10.1093/mnras/283.1.193>. arXiv: astro-ph/9607015 [astro-ph].
- Zhang, W., K. Jahoda, J. H. Swank, E. H. Morgan, and A. B. Giles. 1995. Dead-Time Modifications to Fast Fourier Transform Power Spectra. *ApJ* 449 (August): 930. <https://doi.org/10.1086/176111>.
- Zhao, Qing-Chang, Lian Tao, Han-Cheng Li, Shuang-Nan Zhang, Hua Feng, Ming-Yu Ge, Long Ji, et al. 2024. The First Polarimetric View on Quasiperiodic Oscillations in a Black Hole X-Ray Binary. *ApJL* 961, no. 2 (February): L42. <https://doi.org/10.3847/2041-8213/ad1e6c>. arXiv: 2401.08970 [astro-ph.HE].